Smart Shunt for Intracranial Pressure Monitoring and Compliance Estimation

By

Chenxiao Guan

A dissertation submitted in partial fulfillment of

the requirements for the degree of

Doctor of Philosophy

(Electrical and Computer Engineering)

at the

UNIVERSITY OF WISCONSIN-MADISON

2023

Date of final oral examination: 05/10/2023

The dissertation is approved by the following members of the Final Oral Committee:

Yu Hen Hu, Professor, Electrical and Computer Engineering
Joshua E. Medow, Professor, Neurological Surgery
Bermans J. Iskandar, Professor, Neurological Surgery
Younghyun Kim, Assistant Professor, Electrical and Computer Engineering
Hongrui Jiang, Professor, Electrical and Computer Engineering

Dedicated to my family:
Mom, Dad, Wife, and Son
For their endless love and support.

Acknowledgements

The completion of my dissertation would not have been possible without the assistance and support of numerous individuals. I would like to take this opportunity to express my gratitude to everyone who contributed to this journey.

First and foremost, I would like to extend my deepest thanks to my advisors, Professor Joshua E. Medow, and Professor Yu Hen Hu, for their unwavering support and encouragement in my research. They guided me into the fascinating realm of neurology and hydrocephalus, which, given my background in computer engineering, was a complex and challenging transition. They consistently offered guidance and solutions to any obstacles I encountered, patiently addressing my questions, reviewing my work, and providing invaluable advice. I am also grateful to my committee member and project PI, Professor Bermans J. Iskandar, for his support throughout my PhD journey.

Furthermore, I want to express my appreciation for the professors and members of our research group. Professors Christopher Luzzio, John G. Webster, and David Hsu provided constructive feedback on the smart shunt design. Without Professor Christopher Luzzio's assistance, the brain compliance simulation platform would not have been possible. Fa Wang, my mentor upon joining the WHP group, taught me how to develop embedded medical devices. Xuan, as an experienced lab member, offered significant support during my early days in the WHP group. Zhe Yang, Quan Chen, Joyce, and Roy, as team members across both engineering and clinical aspects, provided steadfast support throughout my PhD journey.

I am grateful to my friends in Madison, including Yijing Zeng, Cheng Liu, Fei Men, Lei Zhao, Di Wu, and others, for the cherished memories that have energized me during challenging times.

I would also like to thank Professor Yanzhi Wang, my mentor at USC, and the many talented friends and mentors I have encountered who have contributed to my personal growth.

Lastly, I want to convey my most profound gratitude to my family. My wife, Jiarui Zhang, has provided unwavering support, helping me maintain focus on my research. I am grateful to my parents, Zupei & Jun, and my parents-in-law, Huimin & Hong, for caring for our son when we were occupied with our research. Finally, I want to thank my son, Ethan Guan, whose presence has inspired me to work diligently and persevere – to become a father he can learn from.

Abstract

Hydrocephalus is a medical condition characterized by an excessive buildup of cerebrospinal fluid (CSF), resulting in elevated intracranial pressure (ICP) that can cause headaches, cognitive impairment, and even death. To address the limitations of conventional treatment methods, a smart shunt is developed to relieve the elevated ICP. It is an implantable device that minimizes the risk of over-drainage and has a lower failure rate compared to traditional shunts. The smart shunt includes a sensor reader circuit, a valve driver circuit, and a control circuit, and is equipped with a custom-made pressure sensor that measures ICP and a piezo-actuated shunt valve that can be controlled with high voltages (±100V). The smart shunt utilizes a novel control algorithm that opens the valve when the average ICP exceeds the upper threshold and quickly closes it when the instantaneous ICP falls below the lower threshold, effectively preventing over-drainage.

We performed experiments on a physical ICP simulation platform and generated ICP waveforms for analyzing brain compliance, which is a crucial indicator for assessing hydrocephalus but has been difficult to measure reliably until now. ICP waveforms corresponding to 22 simulated patients were generated under varying brain conditions, ICP base pressures and heartbeat rates. Using these recorded ICP waveforms, we developed two models for estimating brain compliance using the ICP waveform over a cardiac cycle: one based on the P2/P1 ratio and the other using the area under the curve combined with baseline pressure. The models differ between patients but can be correlated, allowing for further investigation into the relationship between these correlations and their implications for monitoring compliance values.

Contents

Chapter 1: Intracranial pressure and its monitoring

1.1 Background

Hydrocephalus is a medical condition characterized by an excessive buildup of cerebrospinal fluid (CSF), resulting in an abnormal increase in intracranial pressure (ICP). This condition, which can affect both children and adults, is often present at birth. Hydrocephalus impacts 1 to 2 out of every 1000 live births, making it the primary reason for brain surgery in children in the United States. The National Institutes of Health (NIH) estimates that 700,000 children and adults are living with hydrocephalus, though fewer than 20% are accurately diagnosed. The annual medical cost of hydrocephalus exceeds US$ 1 billion. While the introduction of CSF shunting in the early 1900s and one-way valve systems in the 1950s has saved countless lives, CSF shunt systems have seen minimal improvement over the past six decades. Improved treatments enhanced long-term monitoring, and accurate, low-cost, noninvasive diagnostic tests are necessary (Hydrocephalus Association 2016).

The abnormal accumulation of CSF can lead to headaches, cognitive impairment, and even death. Once hydrocephalus is detected, treatment options may include endoscopic procedures to restore proper CSF flow or the insertion of a ventriculoperitoneal (VP) shunt to alleviate increased ICP by diverting the fluid to other body cavities such as the pleural space, cardiac atrium, or most commonly, the peritoneum. Prompt identification of elevated ICP is crucial to

minimize the risk of permanent brain damage and to effectively manage hydrocephalus symptoms throughout the patient's life.

1.2 Physiology and pathophysiology of intracranial pressure

Intracranial pressure (ICP) refers to the pressure within the cranial cavity, typically measured in mmHg and referenced to atmospheric pressure. Normal ICP values differ based on age and body position, ranging from 5 to 15 mmHg in supine adults, 3 to 7 mmHg in children, and 1.5 to 6 mmHg in term infants (Smith et al. 2008, Raboel et al. 2012).

ICP is significantly impacted by the equilibrium of volumes within the brain (1100 to 1300 cm^3), cerebrospinal fluid (CSF) (130 to 150 cm^3), and blood in intracranial vessels (60 to 80 cm^3). As brain volume remains relatively constant (except under conditions that may cause cerebral edema or hemorrhage), CSF and intravascular blood are the primary determinants of ICP. Cerebral blood flow is mostly stable and depends on mean blood pressure. Abnormal ICP may result from an imbalance between CSF production in the brain ventricles and its absorption into the dural venous sinuses (Mokri et al. 2001, Popovic et al. 2009).

Cerebral perfusion pressure (CPP), or the blood pressure within the brain, is generally consistent in healthy individuals due to autoregulation (Steiner and Andrews et al. 2006). CPP is calculated as the difference between mean arterial blood pressure (MAP) and ICP (CPP = MAP - ICP). When ICP is elevated, CPP decreases. As such, CPP is an important parameter to monitor and maintain when addressing increased ICP (Steiner and Andrews et al. 2006, Duschek and Schandry et al. 2007).

Elevated ICP can result from various medical conditions, including intracranial mass lesions, hydrocephalus and other CSF circulation disorders, more diffuse pathological processes, and

head injuries causing intracranial hematoma or cerebral edema. Increased ICP can lead to compression and damage of brain structures, brain herniation, and reduced blood supply to the brain (Graham et al. 2000, Steiner and Andrews et al. 2006).

1.3 Role of ICP monitoring in current clinical practice

ICP monitoring is a crucial component in the management of various medical conditions, serving as a valuable tool in clinical practice to assess brain pressure and compliance (Di Ieva et al. 2013). However, the field currently lacks standardized guidelines, leading to hospitals adopting different ICP monitoring practices (Raboel et al. 2012).

Continuous ICP monitoring is employed in the treatment of severe closed head injuries in both adults and children (Dunn et al. 2002), as well as subarachnoid and other brain hemorrhages, meningitis, cerebral edema caused by acute liver failure, stroke, benign intracranial hypertension, craniosynostosis (head shape deformities), and issues related to hydrocephalus and CSF shunt function (Czosnyka and Pickard et al. 2004).

There is now an urgent need to research and incorporate ICP monitoring into a comprehensive, personalized approach to clinical care (Hawthorne and Piper et al. 2014), utilizing patient-specific parameters for ICP and CPP. Both invasive and non-invasive ICP monitoring techniques have been developed for application in a range of clinical situations.

1.4 Invasive ICP monitoring

Invasive methods are considered the standard approach for direct ICP monitoring. There are various invasive techniques for measuring ICP, which can be performed at different intracranial

anatomical locations: intraventricular, epidural, subdural, subarachnoid, and intraparenchymal. Additionally, in certain situations, ICP may be assessed via lumbar puncture in patients with communicating CSF pathways (Eide and Brean et al. 2006, Lenfeldt et al. 2007, Speck et al. 2011).

ICP measurements can be taken at multiple brain sites. Intraventricular and intraparenchymal measurements are more frequently used, while extradural and subdural measurements are less common due to their measurement inaccuracies. The standard invasive technique involves inserting a catheter into the ventricular system, typically through a small hole drilled in the skull. Alternatively, a pressure probe or sensor can be placed within the brain parenchyma (Zhong et al. 2003, Ross and Eynon et al. 2005, Rai and Varadan et al. 2010, Kashif et al. 2012).

1.5 Noninvasive ICP monitoring

Various invasive ICP measurement methods are available, but there is a need for a noninvasive ICP (nICP) monitoring system with clinically acceptable accuracy. Noninvasive ICP measurement is appealing for two reasons: (1) it minimizes complications associated with invasive methods, such as hemorrhage and infection; and (2) it enables continuous long-term ICP measurements without requiring a new device to be inserted each time a measurement is needed due to clinical changes, a procedure that can only be performed by a neurosurgeon in a specialized facility. Partial information can be obtained through magnetic resonance imaging (MRI), ultrasound, or Doppler flow (Rosenberg et al. 2011). The correlation coefficient between nICP and ICP indicates how well ICP can be predicted using nICP. Several methods for nICP monitoring have been proposed (Popovic et al. 2009, Kashif et al. 2012), which generally measure physiological variables that indirectly correlate with ICP.

Numerous non-invasive methods have been suggested and developed for nICP monitoring, which can be grouped into five broad categories: Fluid dynamic, Ophthalmic, Otic, Electrophysiologic, and other. Fluid dynamic-related methods include magnetic resonance imaging (MRI), transcranial Doppler ultrasonography (TCD), cerebral blood flow velocity (CBFV), near-infrared spectroscopy (NIRS), and transcranial time-of-flight, all of which assess dynamic fluid changes in ICP, cerebral blood flow, and cerebral compliance. Ophthalmic-related methods involve spontaneous venous pulsations (SVPs), venous ophthalmodynamometry, optical coherence tomography (OCT) of the retina, optic nerve sheath diameter (ONSD) assessment, and pupillometry. The eye serves as a window to the cranial vault due to the dural extension of the optic nerve sheath and the communication between perioptic nerve CSF and cerebral CSF (Bruce et al. 2014). Otic-related methods include sensing tympanic membrane displacement (TMD), analyzing otoacoustic emissions (OAE)/acoustic measures, and transcranial acoustic (TCA) signals. The ear has an indirect communication with CSF, allowing for ICP evaluation via the cochlear aqueduct, which provides pressure relief for the inner ear between the perilymph of the cochlea and posterior cranial fossa CSF. Electrophysiologic-related methods, such as visual-evoked potentials (VEP) and electroencephalogram (EEG), can predict elevated ICP using nICP based on the slowing of cerebral electrical activity. Other non-invasive methods under development include skull vibrations, brain tissue resonance, and jugular venous outflow. While all these non-invasive methods for determining ICP are generally inaccurate, they can provide insights into ICP elevation in a broader sense.

1.6 Components of ICP waveform

One way to directly assess cerebral compliance without additional risk is through ICP pulse waveform analysis. This method does not require the placement of any additional devices beyond the pressure sensor. The waveform primarily originates from pulsations of intracranial arterial inflow, with contributions from CSF reverberation from the lumbar cistern and retrograde venous pulsations. Analyzing the components of the ICP waveform can help determine a patient's compliance status.

A single ICP waveform consists of three peaks (P1, P2, and P3) that correlate with the propagation of arterial pulse pressure (Figure 1.1). P1, also known as the systolic or percussion wave, is produced by the transmission of arterial pressure. When the shockwave reaches the ventricular system, ventricular compression creates the CSF pulse wave, generating P1 and forcing CSF through the ventricular system's outlets via the foramina of Magendie and Luschka (Stephen et al. 2014) into the subarachnoid space surrounding the brain and spinal cord. Following ventricular compression, ICP decreases as some CSF is expelled from the ventricular system. As the arterial pulse pressure further propagates into the brain parenchyma, ICP rises again due to the succussion splash, which is P2. ICP decreases with a decline in arterial pressure and volume and venous blood outflow, then the pressure transmission of aortic valve closure generates the dicrotic wave, which is P3.

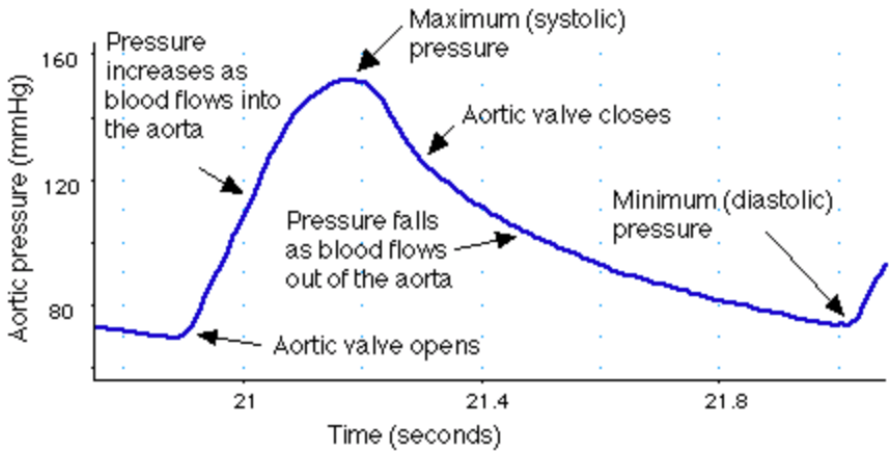

Figure 1.1: Transmission of arterial pressure.

P1 typically has a higher amplitude than P2. However, when intracranial volume and pressure increase and brain compliance decreases, P2 may surpass P1. This indicates reduced brain compliance and impending herniation (Figure 1.2). With low brain compliance, there is less CSF in the subarachnoid space to be expelled, altering the ICP waveform shape and eventually causing P2 to be higher than P1.

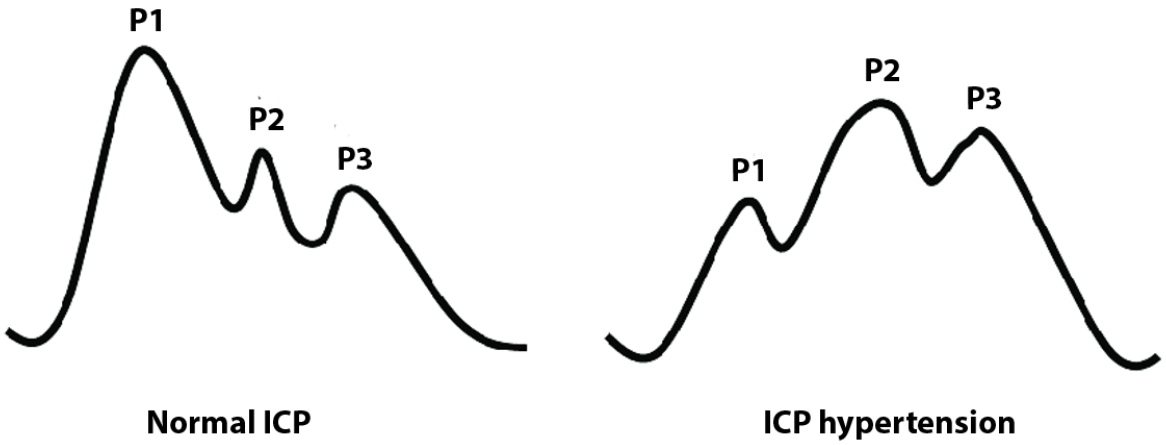

Figure 1.2: Intracranial pressure waveforms under normal (left) and low (right) compliance.

Recent research indicates that ICP pulse amplitude (AMPICP) serves as a more effective marker than mean ICP in various conditions, such as hydrocephalus, traumatic brain injury (TBI), and subarachnoid hemorrhage (Carrera et al. 2010; Eide et al. 2006; Holm et al. 2008). Additionally, experimental studies suggest that ICP pulse amplitude is influenced by both mean ICP and cerebral arterial blood volume (AMPCaBV) (Carrera et al. 2010). Given that the area under the curve in each cardiac cycle is also affected by cerebral arterial blood volume, brain compliance may be determined based on ICP waveform information, such as mean ICP and the area under the curve (Figure 1.3), as long as cardiac pulse volume variability is minimal. As intracranial pressure increases, it becomes more difficult for blood to enter the head, leading to a reduction in the area under the curve. At a certain point, the initial ICP pressure is too high for blood volume to enter. In cases of exceptional compliance, blood can easily enter, resulting in a small area under the curve. This occurs during a craniectomy, where compliance is significantly improved due to the removal of a part of the skull. The area under the curve is more of a function of compliance between low and high compliance levels. To differentiate between high and low compliance, mean ICP measurement can be used. If mean ICP is high and there is no area under the curve, compliance is poor. Conversely, if the intracranial pressure measurement is low and there is no area under the curve, compliance is high. The area under the curve increases to a point as compliance decreases, then decreases. When compliance is poor, blood flow drops dramatically. In extreme cases, Δp from peak systolic pressure to end-diastolic pressure reaches zero.

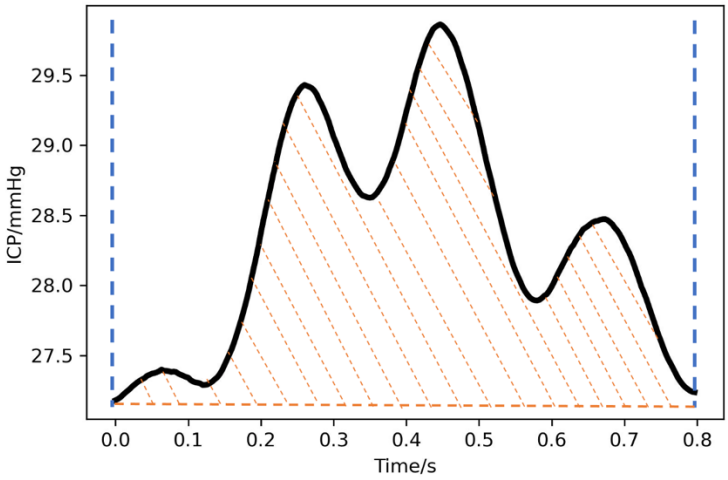

Figure 1.3: The area under the curve represents the area of ICP waveform above the baseline pressure in one cardiac cycle.

A semi-automated algorithm has been developed to identify P1 and P2 values based on each pulsation. The baseline pressure is captured by the local minima. Using ICP waveform information and baseline pressure, the area under the curve for each pulsation can be calculated.

1.7 Future of intracranial pressure monitoring

Intracranial pressure monitoring is a crucial tool for managing conditions such as hydrocephalus, traumatic brain injury, and other neurological disorders. It allows clinicians to obtain accurate intracranial pressure measurements and make informed decisions regarding patient care. However, the development of noninvasive ICP monitors as a critical future direction is currently hindered by technological limitations (Di Leva et al. 2013, Hawthorne and Piper et al. 2014). Existing ICP monitoring systems are invasive, requiring the opening of the skull and the implantation of sensors with wires or catheters that exit the skin to connect to various monitors. Invasive ICP monitoring is associated with complications such as disconnection, device failure, infection, and hemorrhage. Ventricular-catheter related infection rates are approximately 10% and are correlated with the duration of catheter placement (Fried et al. 2016, Lozier et al. 2002). Clinically symptomatic hemorrhages due to catheters range from 0.7% to 2.4% (Fried et al. 2016).

Considering the current limitations of noninvasive ICP monitoring and the numerous complications associated with invasive ICP monitoring, we propose the development of a smart shunt. This device would not only function like a traditional shunt for hydrocephalus treatment but would also provide precise and reliable long-term intracranial pressure monitoring with a reduced failure rate. Advanced features, such as low compliance detection and self-calibration, could further enhance the utility of this innovative solution.

Chapter 2: Smart shunt

2.1 Overview

The smart shunt is an internal device designed to monitor conditions such as ICP or CSF drainage rate and adjust the shunt based on the patient's individual information. Generally, it is defined as an implantable system created to regulate CSF drainage according to data measured either internally or externally. All smart shunt concepts share a common framework: an internal fluid control mechanism, an actuator to operate the valve, one or more sensors (external or internal), a power source, communication capabilities, and a protective casing to separate electrical components from the body.

Our smart shunt is an implantable system for managing intracranial pressure (ICP). Figure 2.1 illustrates the entire system. The microcontroller, internal reader, and valve driver are implanted between the skull and scalp, while the sensor is implanted through the dura layer, with the membrane potentially in contact with the cerebrospinal fluid (CSF). The complete system comprises: a catheter implanted within the patient's brain, with a proximal portion inside the brain and a distal portion diverting CSF out of the brain to another area of the patient's body; a sensor implanted within the brain, generating a signal representing ICP; a valve that allows excess CSF to drain from the brain through the catheter when in an open position, and prevents excess CSF from exiting the brain through the catheter when in a closed position; and a valve driver that receives the signal representing ICP, controlling the valve to alternate between open and closed positions in a cycle for consecutive cycles.

Figure 2.2 displays the primary component block diagram for the Wisconsin Hydrocephalus Project (WHP) smart shunt system. This system comprises a pressure sensor with an internal

reader, microcontroller, driver circuit, piezoelectric actuator, and on/off valve. The pressure sensor, combined with the internal reader, provides a voltage reading based on the ICP sensor value within the patient's head. The microcontroller takes the sensor reading and calculates the moving window average (control algorithm) of these readings over a 60-second period. Using the average ICP, the microcontroller manages the position of the piezoelectric actuator through the driver circuit. The actuator is situated within the on/off valve to regulate the CSF shunt flow (either 0 or positive).

In this project, I collaborated with Xuan on the ICP pressure sensor reader circuit. I designed the smart shunt control algorithm, smart shunt working schedule, and finalized the smart shunt design, resulting in the production of the first prototype.

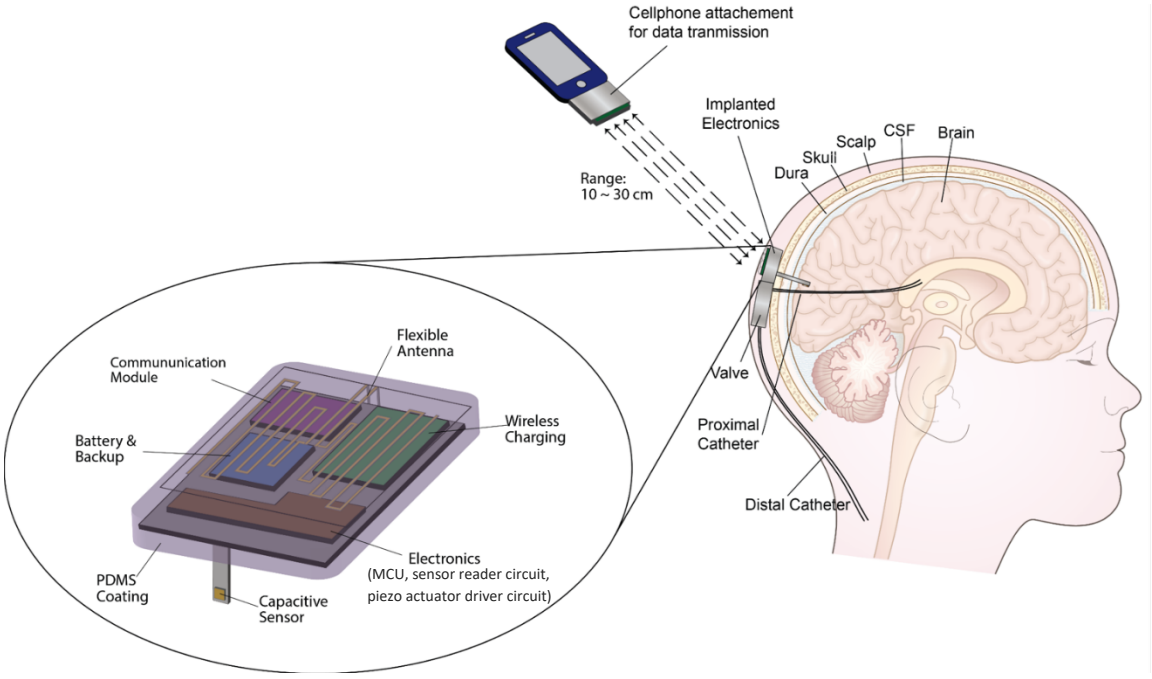

Figure 2.1: ICP management system overview. It consists of telemeter, sensor tag, pressure sensor, valve driver and valve.

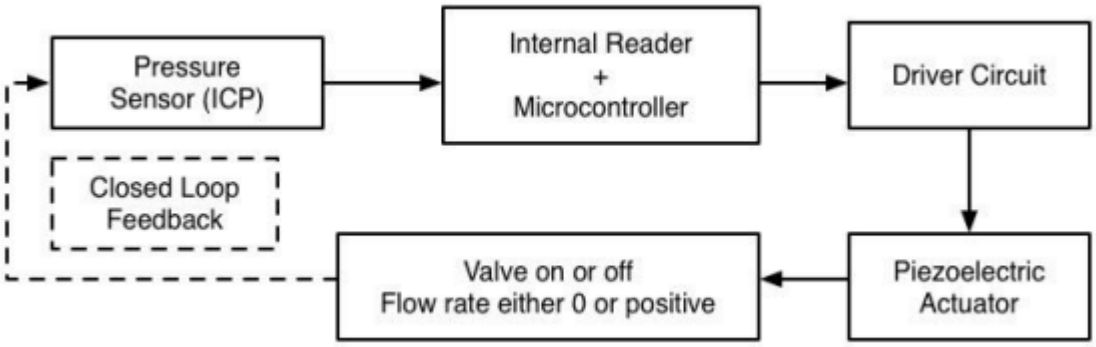

Figure 2.2: The smart shunt system yields a positive flow when the ICP exceeds +13 mmHg.

2.2 Sensor

In this section, I will discuss the work of my colleague, Xuan Zhang, who focused on developing and fabricating an intracranial pressure (ICP) sensor for permanent brain implantation. Xuan successfully fabricated a capacitive silicon sensor at the Wisconsin Center for Applied Microelectronics. The sensor functions by bending a diaphragm as pressure increases, reducing the distance between two plates, and subsequently increasing their capacitance. The enhanced capacitance leads to the storage of digital numbers in the microcomputer memory through a capacitance-to-digital converter. The sensor's dimensions are 4 mm × 6 mm × 0.55 mm, allowing for implantation through a 5 mm diameter skull burr hole and into the ventricle. To protect the sensor from bodily fluids, it is coated with a 10 μm layer of Parylene C. I integrated this internal sensor reader circuit into the smart valve system to monitor ICP.

2.2.1 Sensor reader circuit

A capacitive pressure sensor reader circuit is used to measure pressure changes by detecting changes in capacitance. Due to high resolution, high speed and low power features of FDC2114, I picked FDC2114 (Figure 2.3) as the capacitance-to-digital convertor for detecting the capacitance. An LC tank was applied to set the frequency of oscillation. Based on the sensor

frequency data from SDA, we can calculate the capacitance of our ICP pressure sensor from equation 2.1.

$$C_{sensor} = \frac{1}{L * (2\pi * f_{sensor})^2} - C \tag{2.1}$$

Where C is the parallel sensor capacitance.

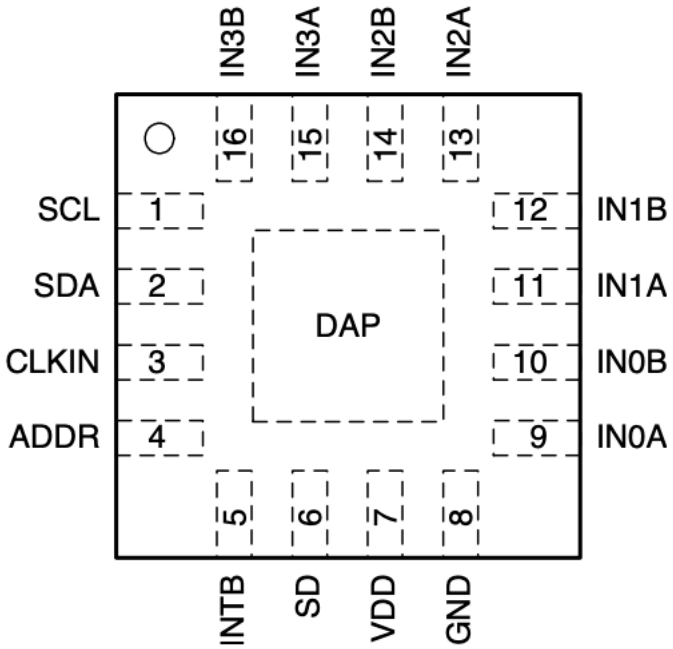

Figure 2.3 FDC2114 RGH package 16-pin WQFN top view from FDC2114 data sheet.

2.2.2 Sensor measurement and test

This section highlights collaborative work with Xuan. The sensor was designed to measure absolute pressures ranging from 550 to 760 mmHg, accommodating ICPs from sea level to pressures experienced in airplanes at 8,000 feet altitude, as well as a high pressure range from 760 to 900 mmHg. Our capacitive sensor's full measurement scale extends from 0 mmHg to 1,000 mmHg, with an accuracy of 0.08% over two months. Figure 2.4 displays the sensor measurement test results for pressures between 500 and 900 mmHg, generated by a movable piston of a syringe. The test results demonstrate the sensor's excellent performance, featuring a

resolution of 0.022 mmHg, drift value of less than ±0.5 mmHg (0.05% FSO), and repeatability across the sensor range for two months.

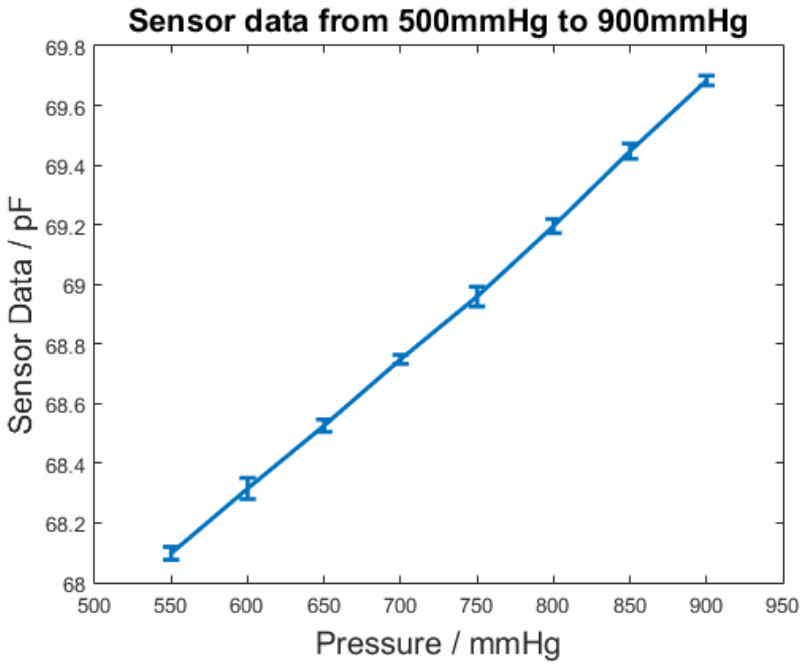

Figure 2.4: Sensor output increases with elevated ICP.

We established the sensor calibration system and sensor long-term test platform to realize accelerated testing for long-term stability and performance distribution consistency. An automatic sensor test platform has been set up as shown in Figure 2.5. With the help of a power supply, measuring cylinder, temperature meter and pulsation/pressure generator, the sensor test platform will yield pressure measurement of the capacitive sensor from 500 mmHg to 900 mmHg automatically and repeatedly without manual control. This sensor test platform will save much time as well as avoid important fluctuations from manual control and environment. Figure 2.6 is a prototype of the capacitance pressure sensor.

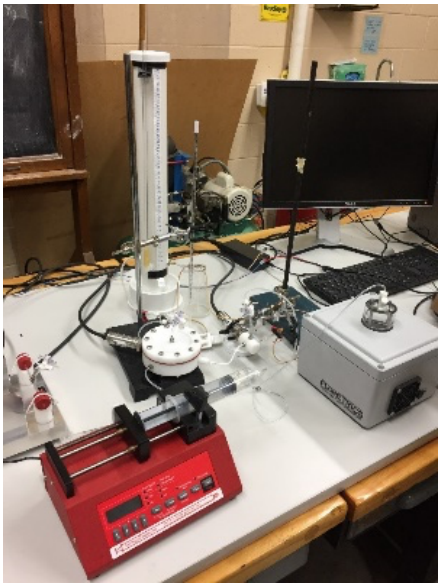

Figure 2.5: Automatic sensor test platform.

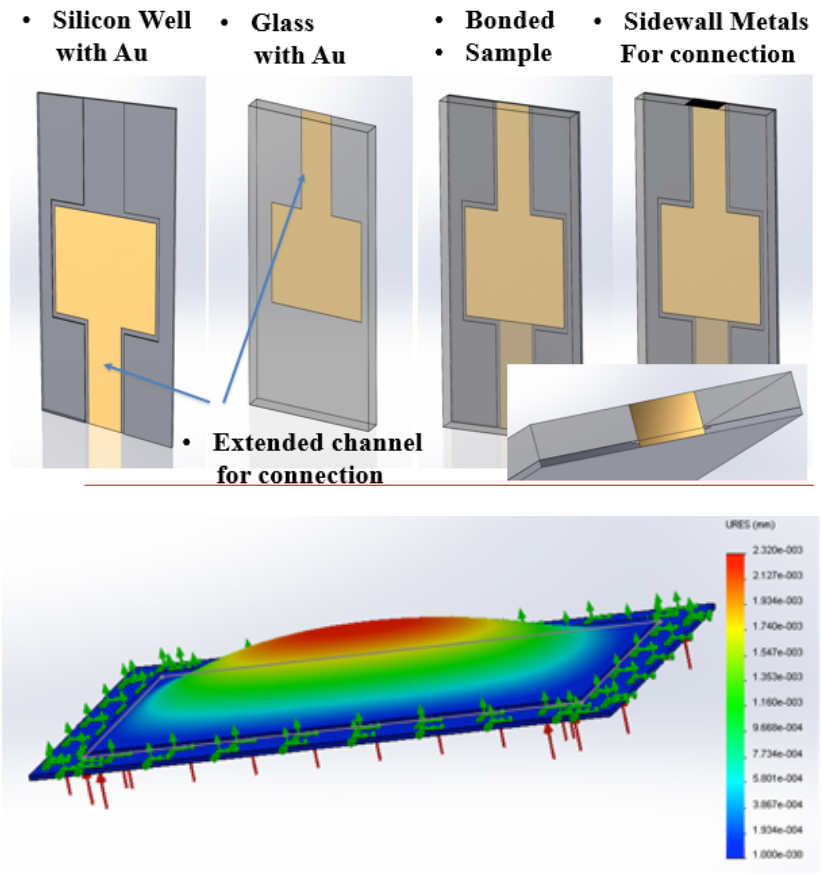

Figure 2.6: Capacitive pressure sensor.

2.3 Valve and valve driver

Prof. Luzzio completed the final design of the piezo-actuated shunt valve utilizing combined CAD and 3D printing technology and machine techniques. The piezo actuator bends and moves a circular valve sleeve surrounding a 1.56 mm diameter stainless-steel hypodermic needle drain tubing with a 0.53 mm diameter hole drilled as a valve orifice. The valve housing is 50 mm × 12 mm × 6 mm. The fabrication technique, design, and size make it easily reproducible and fine-tunable for animal and in-vitro experimentation; the stainless drain tubing can be slid right or left to precisely locate the valve orifice with respect to the valve sleeve as shown in Figure 2.7. Inside the valve, 0.7 mm range piezo bender actuator (BA3502) was picked for low power property and fast response. The housing will be further reduced in size to be placed on the back of the head between the skin and the skull.

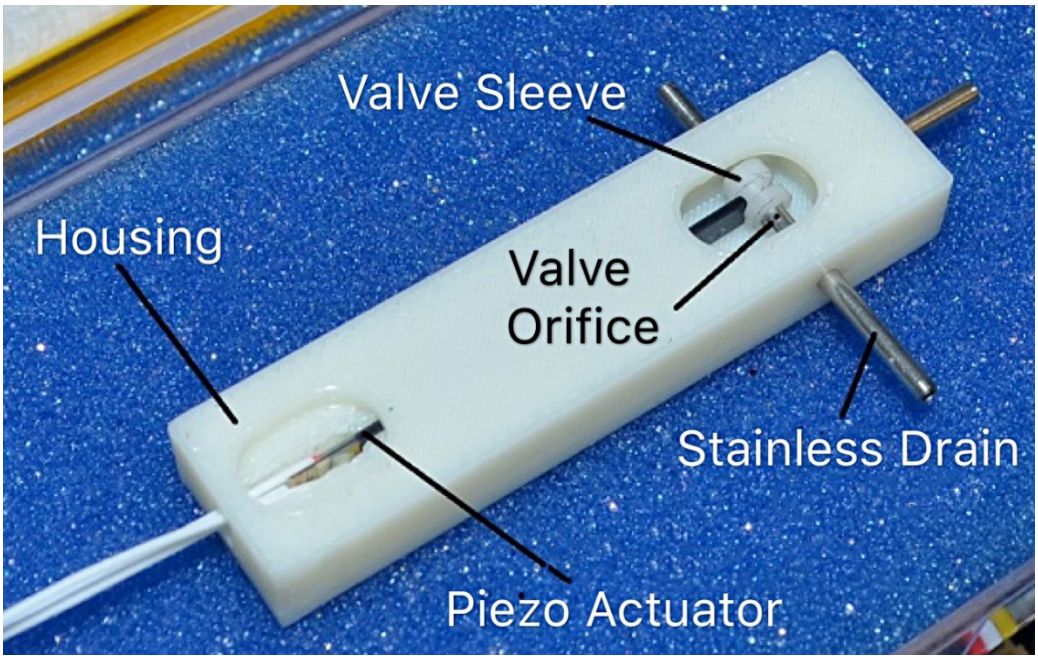

Figure 2.7: Piezo shunt valve.

2.3.1 Valve driver circuit

I designed the valve driver circuit using two-wire method connecting to our piezo bender actuator. The low-voltage piezo haptic driver (DRV8662) was applied into final design due to its high efficiency and high output power. It reduces power consumption and extends battery life for portable applications. It contains an integrated differential amplifier and a booster. It can drive the piezoelectric valve up to 200 V_{pp} with fast transition time. We can set up the boost output voltage using equation 2.2.

$$V_{BOOST} = V_{FB}\left(1 + \frac{R_1}{R2}\right) \tag{2.2}$$

Where $V_{FB} = 1.32\,V$. R1 and R2 are the resistors we set during boost voltage programming (Figure 2.8). It is recommended that the sum of the resistance of R1 and R2 be greater than 500 $k\Omega$.

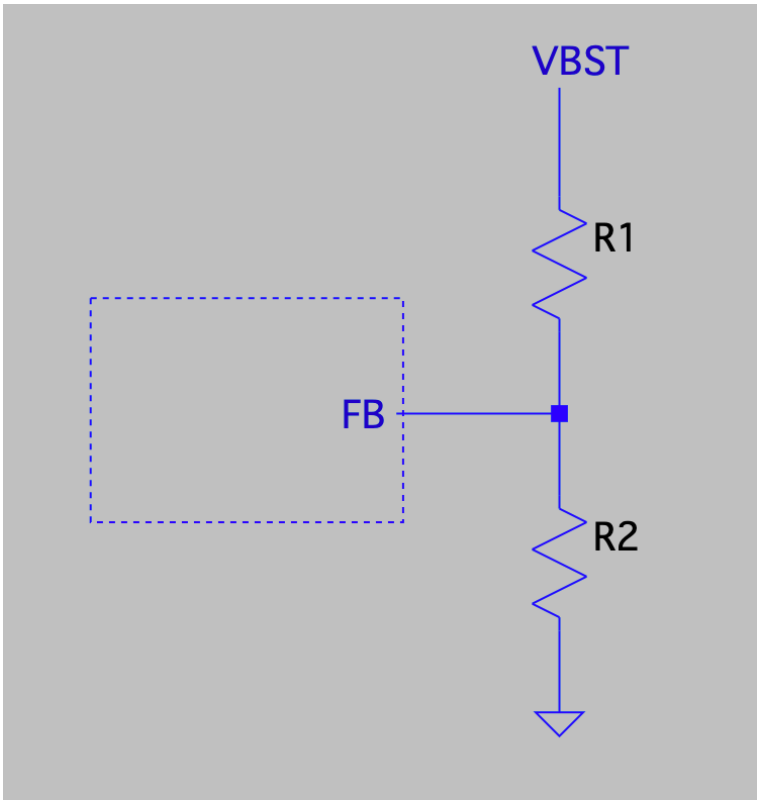

Figure 2.8 Boost voltage programming.

2.4 Control

To perform efficiently, a smart shunt system requires a microcontroller that has an analog to digital converter (ADC) with a minimum sampling rate of 40 Hz for collecting ICP data, the ability to perform a moving window average, a timer that helps to setup the interval window for updating the ICP average value, and the capability of sending an output signal to the control booster circuit according to the ICP average value. I chose this microcontroller, dsPIC33FJ32GP204, for our final prototype. This microcontroller is one of the most popular microcontrollers that can perform complex digital signal processing. It has flash memory with self-programming and self-testing capabilities, and it is designed for low power consumption, with a range of power management features that can help to reduce power consumption and extend battery life for portable applications.

2.4.1 Control algorithm

The ICP waveform has unique characteristics, a single pulse within the ICP wave can consist of up to five peaks P*i*. Physiological parameters of specific patient determine the amplitude and the frequency of each ICP pulse components. Figure 2.9 (Elixmann et al. 2012) shows a typical ICP single wave which is called “P wave”. As introduced in section 1.6, the first three peaks usually are more dominant: P1 is due to the arterial pulse, P2 is due to cerebral compliance, and P3 is due to closure of the aortic valve, which causes the dicrotic notch.

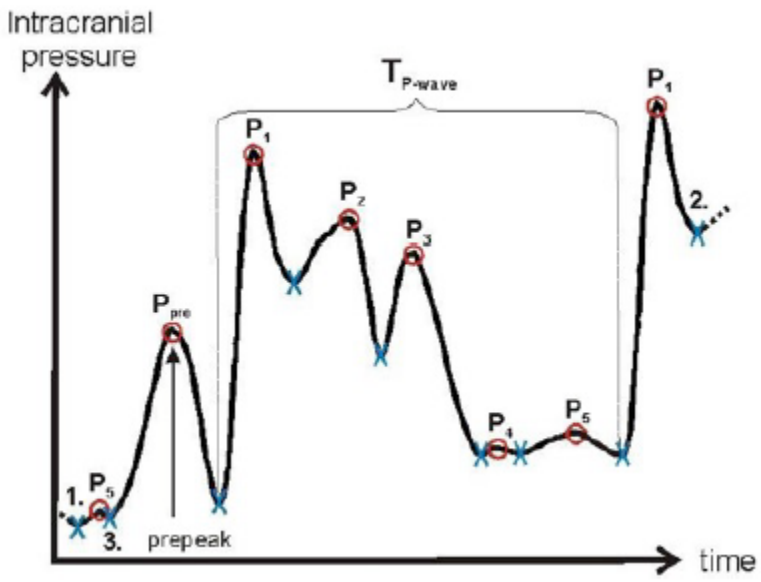

Figure 2.9: A typical single pulse ICP waveform due to heartbeat.

According to (Elixmann et al. 2012), an exponential pressure–volume (*P–V*) relationship exists as follows:

$$\mathrm{ICP}(t) = p_0 + k_0 e^{k_{elast} V(t)} \tag{2.3}$$

Thus, changes in blood volume alter ICP. ICP oscillations may occur as a function of pulsating blood flow to the brain caused by heartbeats (P waves). Numerous proposals have been put forth to discuss the control of a closed-loop shunt system. These control methods for opening and closing the valve can be categorized into three parts: approaches utilizing real-time ICP characteristics, approaches incorporating a combination of real-time ICP characteristics and patient feedback, and approaches using an ICP dynamics model with real-time ICP measurements. However, no specific valve management technique has demonstrated superiority over others, indicating that further studies on existing and new techniques are necessary.

2.4.2 Moving window average

The moving window average is one of the simplest-classical ways to smooth data. It consists of averaging consecutive data through a fixed moving window. The moving interval always is less than the size of the window. For example, six numbers sample size with two numbers moving window as described below. It is a common practice to apply moving window average for improving signal to noise ratio SNR (noise filtering). Figure 2.10 demonstrates a signal with high frequency components has been smoothed after applying moving window average. Figure 2.11 shows an ICP measured through a complete day. It is evident that numerous spikes occur throughout the day. These spikes will open the valve with normal pressure differential valves (which will cause over-drainage over a long period). However, a smart shunt system with moving window average would not be greatly affected by these spikes.

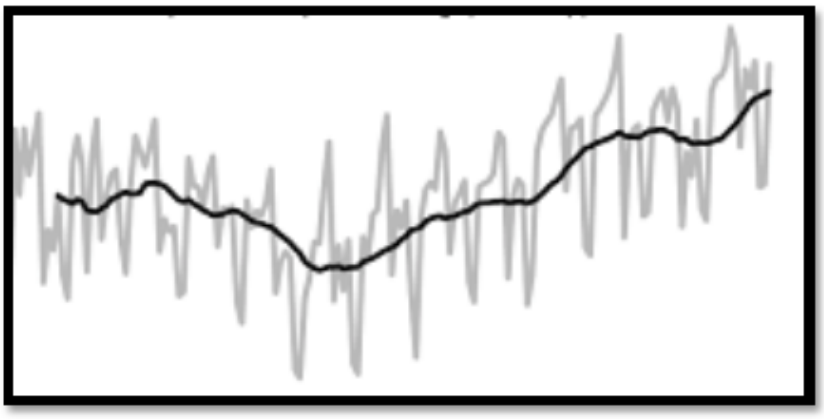

Figure 2.10: High frequency signal with moving window average. (Shmueli et al. 2011)

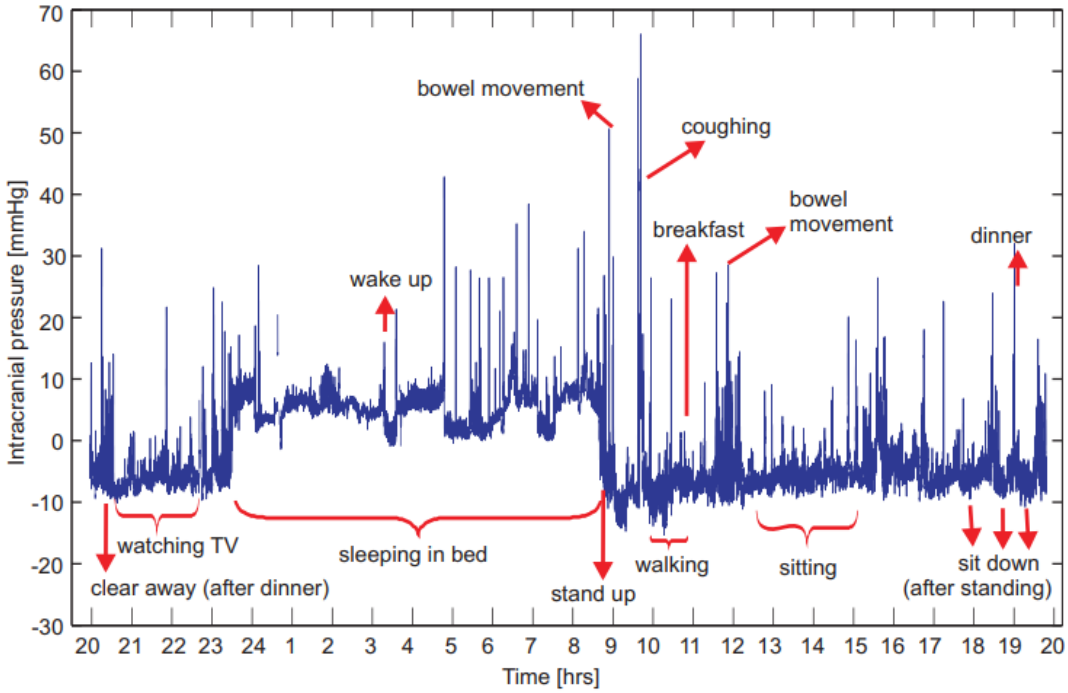

Figure 2.11: Intracranial pressure course over 24 h daily routine at home. (Elixmann et al., 2012)

2.4.3 Program simulation

A simple moving average program uses a Microchip microcontroller. This program collects the ICP sensor capacitance readings for 1 min then calculates the average of these readings. Using the average value, the microcontroller sends the output signal to the driver circuit which in turn opens/closes the valve, if needed. The average value is updated each 1 s by removing the oldest 1 s from the 1 min value and adding new 1 s data, using a moving average algorithm. Figure 2.12 shows the flow chart of this control algorithm. When the average value is larger than the upper threshold, the device would open the valve. When the instant ICP value smaller than the lower threshold, the device would close the valve immediately to prevent over-drainage. Figure 2.13 shows ICP data collected from patients, and the effect of applying a low pass filter on these data. From these data, we can see high-frequency noise has been removed effectively and get a smoother and more stable signal.

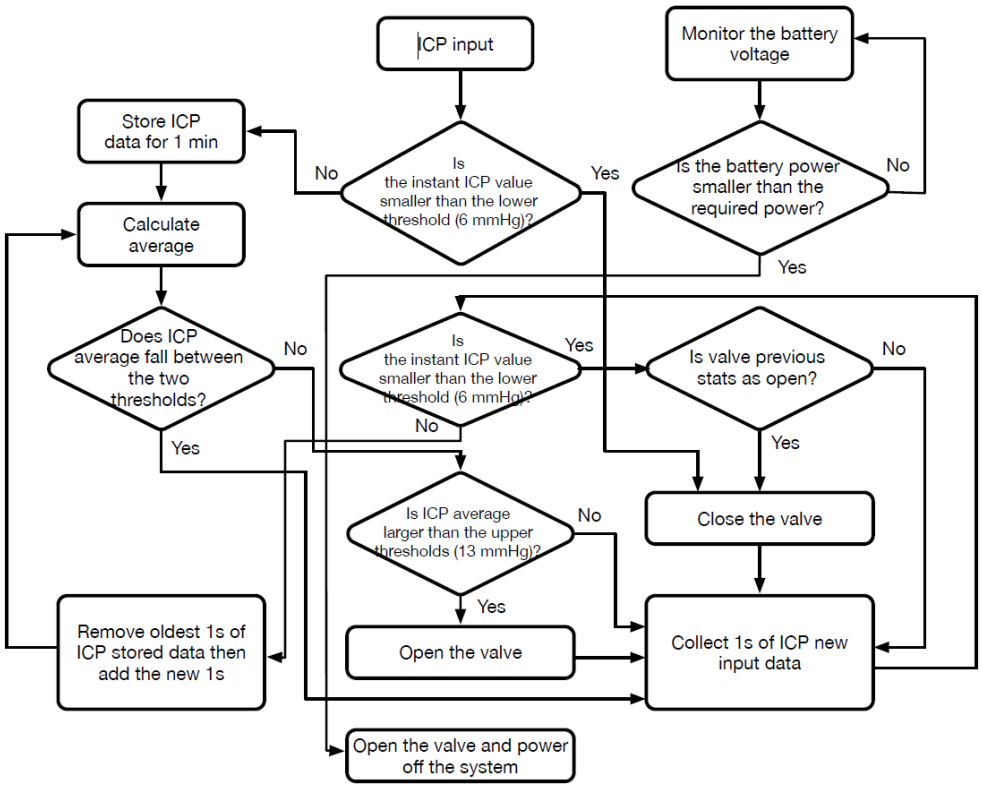

Figure 2.12: Smart shunt control algorithm flowchart.

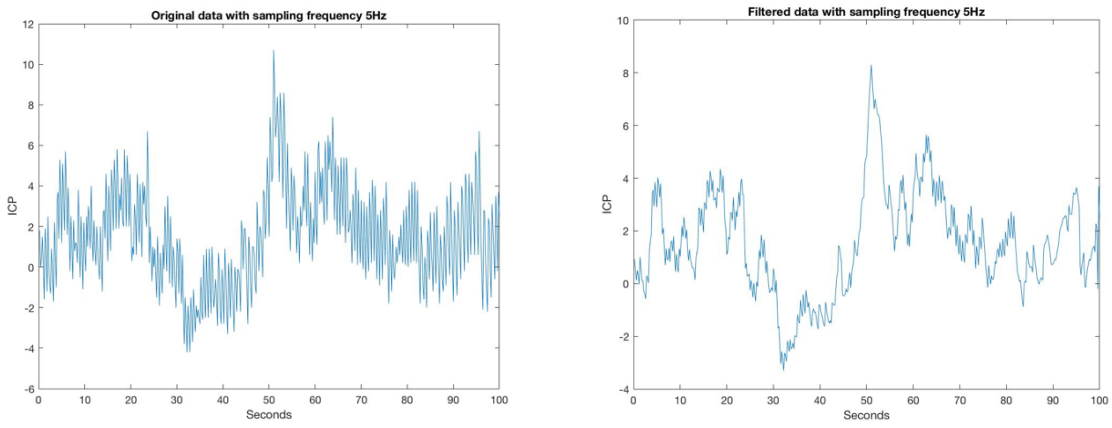

Figure 2.13: Left: Original data; Right: data after applying low pass filtering. (Sampling frequency is 5 Hz.).

2.4.4 Conclusion

There is a tradeoff between the quality of control and the energy consumption. Complex algorithms require more microcontroller tasks that consume energy. Also, there have not been

studies that approve the viability of such complex algorithms. Therefore, a simple moving window average has been selected. This algorithm has been carefully optimized and smooths most ICP sudden changes or spikes (These spikes might cause unnecessary opening/closing the valve).

There are no previous studies that determine the best algorithm to use. We have chosen the moving window average as a control algorithm for the WHP smart shunt system. This algorithm is simpler than other algorithms, and thus easier to implement and consumes less energy. This control algorithm needs to be tested and optimized with a complete closed loop smart shunt system. Also, other groups' algorithms could be tested to make a comparison in the future.

2.5 Power consumption

2.5.1 Power requirement for smart shunt system

Low power consumption is essential for smart shunts to allow operation on battery power for at least a couple of years. Hardware selections and control algorithm are the two most important features which affect power draw. Smart shunt systems always involve a wide tradeoff range between quality of control and power draw. To minimize power consumption, two criteria are very important; low-power components that draw minimum power and a control algorithm that calls these components into action as little as possible. However, despite the importance of power issues to the viability of smart shunts, there is little on the subject in the literature. Unlike mechanical valves, smart shunt valves have a working mechanism that requires decisions about the ICP reading schedule, the way to evaluate these readings, and the level of the valve response. To adequately filter ICP data (which includes removing undesired transients like cardiac cycles, noise, and pressure spikes), it is necessary to obtain the data for a duration of at least several

seconds. Also, most control algorithms require this duration of data to be able to perform an efficient control task.

On the other hand, more data lead to more power consumption. Therefore, an excellent control strategy fails if power consumption exceeds the capability of the system to deliver such power. For our current prototype, we applied non-rechargeable battery. Zhe, another team member in our group, worked on the wireless charging module for our smart shunt supporting rechargeable battery.

2.5.2 Different control strategies

Although control strategies are essential for closed loop shunt systems, there are no major quantitative studies except of two research groups. The group (Al-Nuaimy et al. 2011) defined a figure of merit using computer models to determine the best scenario for opening/closing a smart shunt valve. Their result suggests a total drainage of 15 min/h, which spreads over four intervals. Another research group (Lutz et al. 2013) predicts that if ICP must be maintained within 1 cm H_2O (~ 0.7 mmHg) of a set point, a normally closed position on/off valve requires activation every few minutes. However, according to WHP team, smart shunt valve could be activated in slower rate (once each 1-6 h).

2.5.3 Calculations of power consumption

There are main points related to power management strategy. These are the type of the battery (nonrechargeable vs. rechargeable), the location of the implantation (near the brain surface if there is power/information transmission involved), and the control algorithm. This section describes a brief power consumption calculation for WHP smart shunt system. Table 2.1 shows power budgeting of main components for WHP smart shunt system. Table 2.2 shows one power budgeting example. The driving circuit is only in the active state during transition from opening

to closing and vice versa. Wireless power transfer platform was developed by Zhe for wirelessly charging the rechargeable battery in our smart shunt.

System components	Current Draw	Time Required (s)
Internal Reader		
Capacitance-to-Digital Converter	2.1mA (active) 35uA (sleep)	10s each sampling
Piezo Driver		
Booster Circuit	75mA	2.5ms each activation
Microcontroller		
PIC33FJ32GPXXX	25mA (active) 25uA (idle)	Depends on schedule

Table 2.1: Power budgeting of main components for WHP smart shunt system.

Mode	Time in Mode × # of occurrences during (1 h)	Current		Charge Current * Time (mA s)
		By Device	Mode Total	
Sleep **MCU Idle** **Sensor Off**	(3600s – 2.5ms*3 – 10s*10)*1	 25uA 35uA	60uA	210mAs
Booster **MCU Run** **Driver On**	2.5ms * 3	 25mA 75mA	100mA(500mA)	0.75mAs (3.75mAs)
Sample **MCU Run** **Sensor On**	10s * 10	 25mA 2.1mA	27.1mA(58mA)	2710mAs (5800mAs)
Average Charge during 1 h				2920.75mAs(6013.75mAs)
Total Battery Lifetime in hours = Battery Capacity (50 mAh) / Average Charge in 1 h				61.6hours(29.9hours)
Total Battery Lifetime in days				2.6days(1.2days)

Table 2.2: WHP smart shunt system power budgeting example.

2.6 Final prototype

We built our first prototype with the design above. Figure 2-14 and Figure 2-15 shows the schematic and PCB layout for the electronic part of our smart shunt. Figure 2-16 shows the final device I designed and built. Its function has been fully tested and verified. The whole system consists of a pressure sensor with internal reader, microcontroller, driver circuit, piezoelectric actuator, and on/off valve. Based on our prototype, under our current monitoring schedule, our smart can work over 2 days with a single charge.

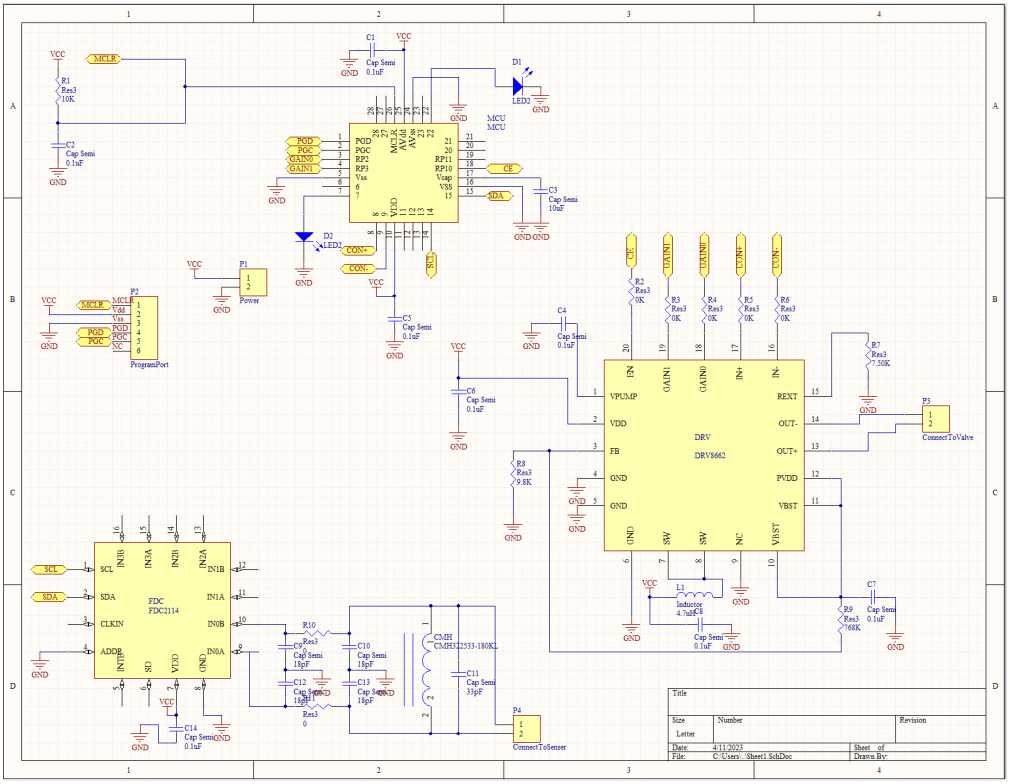

Figure 2-14: Schematic of our smart shunt.

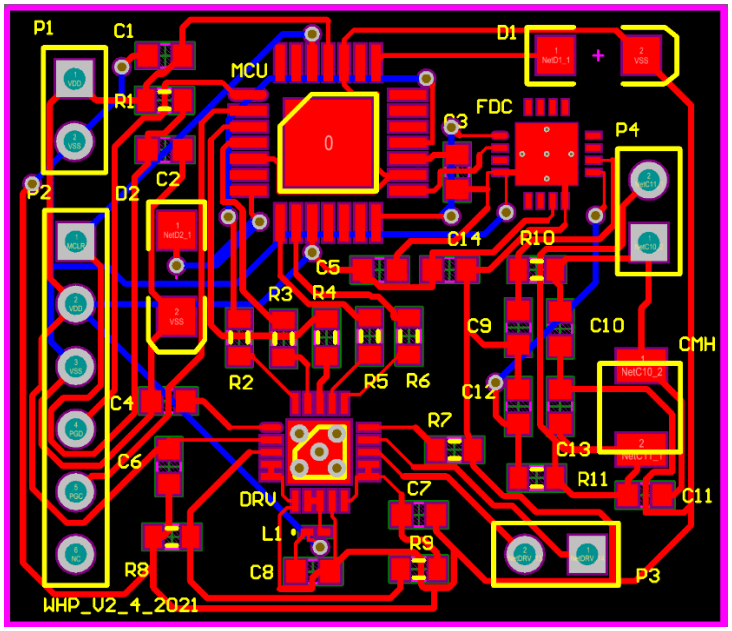

Figure 2-15: Layout of our smart shunt.

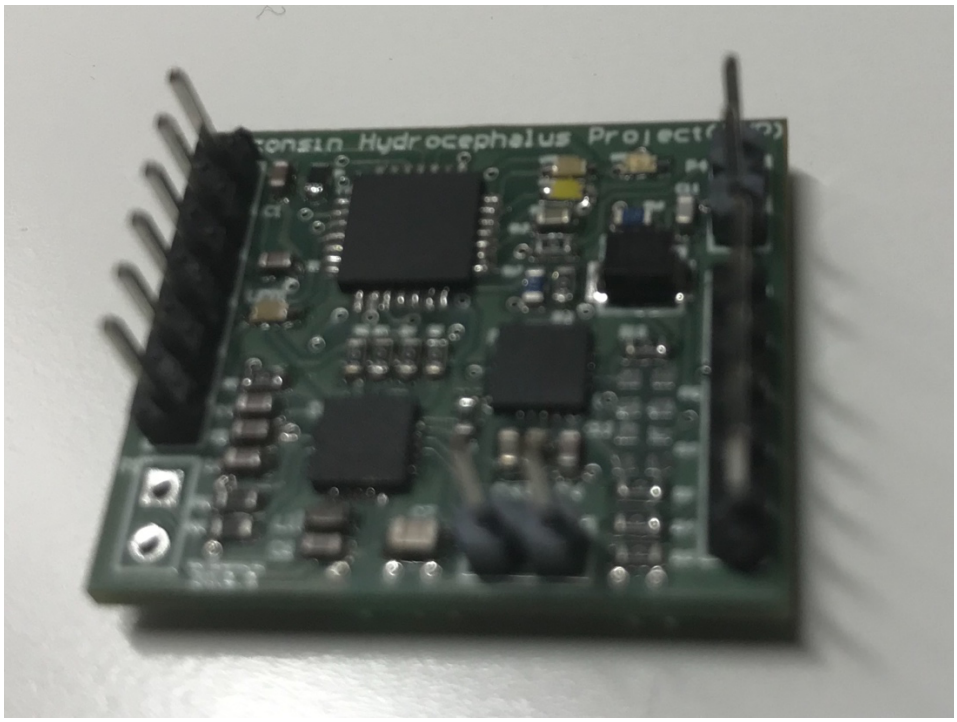

Figure 2-16: Final device integrating the sensor reader circuit, valve driver circuit and microcontroller.

2.7 Conclusion

In this chapter, I designed the sensor reader circuit, valve driver circuit and control circuit for our smart shunt and built our first smart shunt prototype. Our smart shunt can read the ICP pressure from our manufactured ICP pressure sensor (Xuan's work) and generate high voltage value (±100V) to open or close our piezo-actuated shunt valve. With my proposed control algorithm, smart shunt can open the valve when the average ICP value is larger than the upper threshold and close the valve instantly when the ICP value is below the lower threshold to prevent over-drainage. Under our working schedule, when the device is fully charged, it can work continuously for 2.6 days.

Chapter 3: Intracranial compliance estimation based on ICP waveform

3.1 Motivation

Intracranial compliance represents the change in volume per unit change in pressure. It determines the ability of the intracranial compartment to accommodate changes in volume without significant increase in intracranial pressure. This is vital because if the fluid volume inside the skull increases, such as from swelling or bleeding, it can restrict cerebral blood flow and lead to brain damage.

Until now, intracranial compliance cannot be measured directly and reliably. Attempts to employ invasive means to measure the intracranial volume change cannot guarantee that the measurement operation will not impact the accuracy of the results. Many previous attempts have been proposed to estimate the brain compliance using measured ICP value and cerebral perfusion pressure (CPP) (Portella et al. 2005).

In this chapter, we carried out experiments on an ICP simulation platform to assess ICP waveforms and related compliance values to create efficient predictors for brain compliance using two distinct ICP waveform models. The first model relies on the ratio of the peak P1 value to the peak P2 value within an cardiac cycle of the ICP waveform. The second model employs the area under the ICP curve as a function of ICP, in conjunction with baseline pressure. We aim to establish empirical equations for predicting a patient's compliance solely based on ICP waveform measurements.

3.2 Cerebral compliance

The fully fused human skull is a closed non-distensible box. The intracranial space within the skull is composed of three elements: 80% brain tissue, 8% cerebrospinal fluid (CSF), and 12% blood (Germon et al. 1988; Honghao et al. 2020). Cerebrospinal fluid is an ultrafiltrate of plasma contained within the ventricles of the brain and the subarachnoid spaces of the cranium and spine (Sakka et al. 2011; Telano et al, 2021), which performs vital functions, including providing nourishment, waste removal, and protection to the brain (Spector et al. 2015). As Figure 3.1 shows, CSF is mainly secreted by the choroid plexus and, to a lesser extent, by the interstitial compartment. It circulates rostrocaudally inside the ventricles and drains into the cerebellomedullary cistern (cisterna magna) through the median aperture (foramen of Magendie) and the 2 lateral apertures (foramina of Luschka) of the fourth ventricle. CSF circulates in cranial and spinal subarachnoid spaces. In the cranial subarachnoid space, CSF flows towards arachnoid villi in the wall of venous sinuses from which it is absorbed. There is some new literature that may indicate part of the CSF volume is absorbed by the cranial nerve sheaths (optic, trigeminal, facial, and vestibulocochlear nerves) and is drained to some degree by the lymphatic system. In the spinal subarachnoid space, a portion of the CSF may be absorbed by the epidural venous plexus and spinal nerve sheaths en route to the lymphatic system, while the remaining CSF circulates rostrally towards the cranial subarachnoid space. Adult CSF volume is estimated to be 150 ml, with a distribution of 125 ml within the subarachnoid spaces and 25 ml within the ventricles of a normal adult brain (Lauren et al. 2021). ICP is unchanged when the total component volumes remain unchanged. With an increase in volume of one or more of these components, pressure increases as the closed box is unable to enlarge without subsequent decreases in other components.

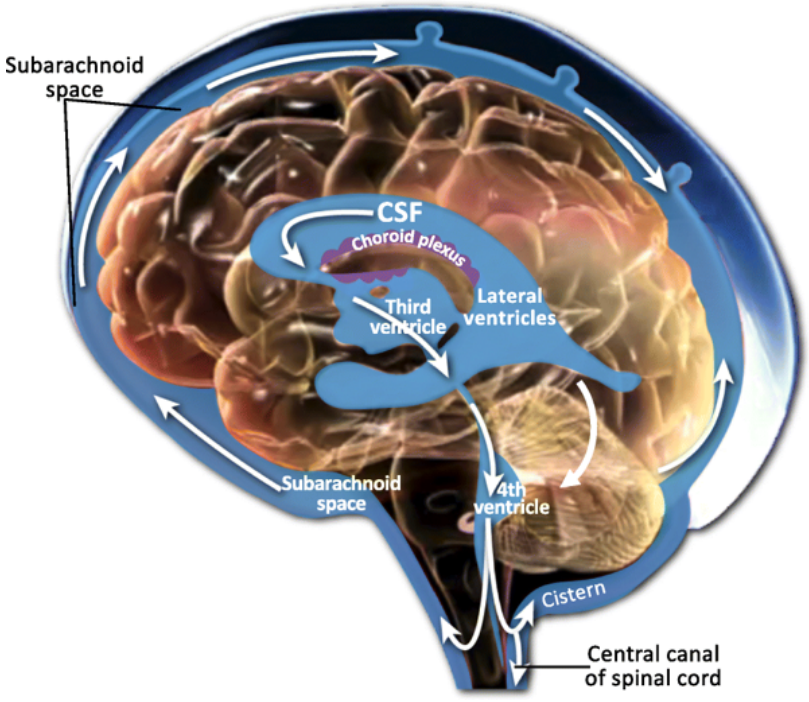

Figure 3.1: Cerebrospinal fluid (CSF) pathway.

Cerebral compliance expresses the amount of ICP pressure increase caused by the intracranial volume change. It is not a global phenomenon but varies in each of 5 cerebral compartments: right and left anterior fossa, right and left middle fossa, and posterior fossa. Cerebral compliance can be written as:

$$C = \frac{\Delta V}{\Delta P} \tag{3.1}$$

C = Compliance, V = Intracranial Volume, P = ICP Pressure

A person with adequate compliance has intact compensatory mechanisms for adapting to an increasing volume (Germon et al. 1988). Once these mechanisms are fully saturated, brain compliance decreases. When a person has low brain compliance, a small increase in the intracranial volume produces a large increase in ICP. For a person with adequate compliance, we can see a normal increase in the intracranial volume from an arterial pulse would result in small

increase in ICP pressure. This phenomenon is described by the volume pressure curve (Figure 3.2) (Germon et al. 1988).

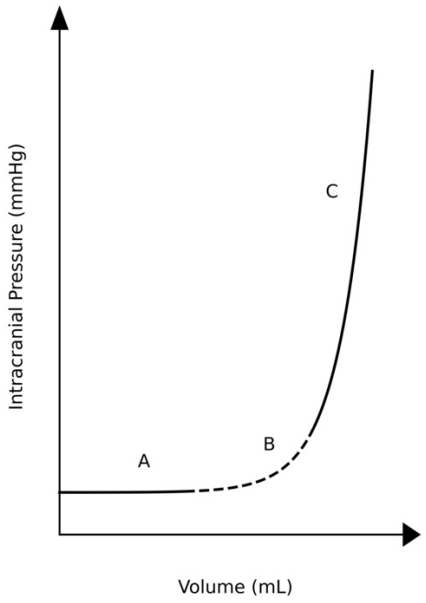

Figure 3.2: Volume-Pressure curve.

Initial increases in volume (area A), can be compensated for so ICP does not increase much. As compensation begins to fail and compliance decreases (area B), small increases in volume result in significant increases in pressure. Clinical symptoms of increased ICP may become apparent in this phase. With continued loss of compensation and decreased compliance (area C), small increases in volume result in exponential increases in pressure. Cerebral circulation is threatened, and herniation syndromes may occur during this phase.

The level of ICP is, therefore, not the only factor which should be considered when evaluating a patient. Compliance can often be the more critical issue. Patients with decreased compliance may sustain greater increases in ICP from a given increase in volume than patients with adequate

compliance. Further, patients with decreased compliance may maintain increased ICP even when volume returns to previous levels. Therefore, patients with decreased compliance are at risk for disproportionate and prolonged increases in ICP in response to a given stimulus. Tissue ischemia, hypoxia, or herniation may follow these increases of pressure.

To illustrate this point, the following example is given. Patient A and patient B both have an ICP of 18 mmHg, slightly elevated, but not a dangerous level in most instances. Patient A has adequate compliance and patient B has decreased compliance. Both patients are placed with their heads flat for invasive line placement. In this situation the resulting decrease in venous outflow from the brain causes an equal increase in intracranial volume for each patient. Patient A's ICP increases to 20 mmHg while flat and rapidly returns to normal when his head is returned to its previous position. Patient B's ICP rises to 30 mmHg and stays greater than 26 mmHg even when his head is returned to its previously elevated position.

Patient B can suffer serious injury from a maneuver that patient A was able to tolerate. If one only considers the actual ICP and not the state of compliance, patients may be subjected to activities beyond their capability to tolerate safely. It is better to know prior to a procedure which patients should be able to tolerate the procedure, and which would probably have problems with increased ICP. Patients identified as having decreased compliance could have additional measures taken prior to a necessary procedure to improve compliance, or low priority procedures could be eliminated.

Another issue pertains to timing of surgery for a failed shunt. If 2 patients had the same mildly elevated ICP but one had poor compliance, it would be clear that depending on the rate of change of compliance that one patient might need air transport and emergency surgery where the other may have much more time to spare.

3.3 Compliance estimation

Clinical methods exist to estimate cerebrospinal compliance, such as the volume pressure response (VPR) test, and the pressure volume index (PVI) (Germon et al. 1988, Shulman et al. 1971). The VPR test measures the change in intracranial pressure induced by the addition or removal of 1 ml of fluid from the ventricles. With the injection of fluid, the normal response is a rise in ICP of less than 2 mmHg. It is considered low compliance when the increase is greater than 2 mmHg. With the removal of 1 ml fluid, a reduction in ICP should occur under normal compliance. The PVI test measures the amount of injected fluid to produce a 10mmHg increase in the patient's ICP. The normal amount of fluid is 25 ml in an adult patient. If the amount of fluid is less than 10 ml, the patient is said to have slit ventricles and associated low compliance. These invasive techniques to determine compliance have serious potential side effects, such as infection, elevated ICP and tissue herniation. Further, they only demonstrate the state of compliance during the time of testing.

However, these clinical symptoms may be delayed, as there is inconsistency in evaluating cerebrospinal compliance. A large increase in ICP indicates low compliance and may cause rapid neurologic deterioration. Unfortunately, rapid neurologic deterioration is often irreversible. It would be ideal to identify patients' poor cerebral compliance before any significant damage occurs (Germon et al. 1988).

The pressure-volume relationship is defined by the formula below:

$$P = P_0 e^{E_0 V} \tag{3.2}$$

Taking log on both sides, we have

$$logP = E_0 V + logP_0 \tag{3.3}$$

Given two different pressure levels, P_1 and P_2, with corresponding volumes V_1 and V_2,

$$E_0V_2 - E_0V_1 = log\frac{P_2}{P_1} \tag{3.4}$$

Denote $\Delta V = V_2 - V_1$, equation (3.4) becomes

$$E_0\Delta V = log\frac{P_2}{P_1} \tag{3.5}$$

In equation (3.5), P_1 and P_2 represent two different pressure levels, not relating to the peaks of in one ICP cardiac cycle.

Anthony et al. (Anthony et al. 1977) showed that the ΔV-logP curve can be approximated by a straight line. The slope of the linear volume-log pressure plot is defined as the pressure-volume index (PVI). In equation (3.6), when the volume is injected into the CSF space, pressure is raised from the initial pressure level, P_0, to the peak pressure P_p.

$$PVI = \frac{\Delta V}{log\frac{P_p}{P_0}} \tag{3.6}$$

With the computation of the PVI, compliance can be evaluated by equation (3.7).

$$C = \frac{0.4343\ PVI}{P} \tag{3.7}$$

From this transformation, it was found that the compliance of the cranial vault is inversely related to the CSF pressure (P) at which it is evaluated, and that the degree to which it is inversely related is proportional to the PVI (Marmarou et al. 1975).

We can use this equation to estimate the compliance if we don't have any accurate way to measure the compliance. However, the accuracy of this method needs more investigation.

3.3.1 Compliance measurement using the smart shunt

As we can see above, measuring the brain compliance of a real patient is still a challenging task. Many invasive techniques can provide direct access to the brain, but they would carry significant risks and are not practical for routine clinical use.

For the smart shunt described in Chapter 2, a ventricular catheter is used to drain the excessive cerebrospinal fluid out of the ventricle. If a flow gauge is available to measure the volume of the CSF fluid discharged by the smart shunt during an episode of high ICP value that triggers the control algorithm to turn on the valve, then together with the difference of the ICP values measured (by the sensor) before the valve is turned on and after the valve is turned off, the compliance value would be evaluated directly using equation (3.1).

Unfortunately, in the current version of prototype, a flow gauge is not included in the smart shunt assembly. We may measure the volume of the CSF fluid discharged during the installation of smart shunt. If not, we must resort to indirect method to estimate the cerebral compliance using only the ICP measurements.

3.4 ICP simulation platform

Brain compliance model has been applied to characterize the relation between ICP waveform, behavior of the cerebrospinal system, and brain compliance. Previous modeling work illustrates the complex interdependence of the various components which control the CSF system (Agarwal et al. 1969). It provides a system analysis approach in developing a mathematical model of the CSF system and based on this model to study the mechanisms about pathophysiological parameters. The electrical capacitors and resistances express the compliances and flow resistances of the systems. Intracranial pressure dynamics were simulated based on differential

equations. Models were developed that focus on anatomical features of the cerebrospinal system. Takemae et al. 1987 focused on the pressure increment. Rekate et al. 1988 developed a mathematical model to simulate CSF flow, and CSF production and absorption. A comprehensive whole-body mathematical model (Lakin et al. 2003) was proposed for intracranial pressure dynamics. This model was far more complex than previous work, and calibration of the numerous model parameters based on experimental data introduces significant overhead into the use of this model for simulations. In 2008, a model (Steven et al. 2008) elucidating many features of intracranial hypertension was presented. The solution of the derived differential equations is then used to predict CSF pressure. However, the complexity of these models is clinically unproven, and the math is too intense for a microcontroller within a smart shunt to be able to calculate.

A mechanical ICP simulation platform has been developed by WHP in the department of Neurological Surgery at UW-Madison. As shown in Fig. 3.3 and Fig. 3.4, on this platform, a rigid chamber is used to emulate the skull. Inside this rigid chamber is a latex balloon. A second compliance chamber connects to the skull chamber via a tube to the left and a pressure head chamber connects to the right side of the skull chamber via another tube. The base brain compliance level is set by the syringe air compliance chamber on the top. At the bottom, a pulse generator implemented with a diaphragm pump connects to the inside of the balloon. Water, emulating the CSF, fills the space inside the skull and outside the balloon, as well as the spinal cord chamber and the pressure head chamber. A picture of the physical realization of the ICP simulation platform is shown in Fig. 3.4.

The pressure head chamber allows the setting of the ICP base pressure. The spinal cord chamber emulates the overflow space of CSF during a ventricular pulse. During a cardiac pulse, fluid is

pumped into the balloon from the pulse generator inflating the volume of the balloon. Since the volume inside the skull is fixed, the excessive CSF inside the skull then will overflow into the spinal cord chamber. The rate and amount of such an overflow depends on the base ICP pressure set by the pressure head chamber, the rate of cardiac heart beats set using the pulse generator, as well as the brain compliance emulated by the volume set inside the air compliance syringe.

At each experiment, a fixed volume inside the syringe is set. The air pressure p and the air volume V inside the syringe can be described by the ideal gas law,

$$pV = constant,$$

Where the constant is a function of temperature. Taking the derivative on both sides, one has

$$d(pV) = Vdp + pdV = 0, \text{ or } \frac{dV}{dp} = -\frac{V}{p}.$$

Referring to equation 3.1, the compliance of the brain is emulated by setting the syringe volume V and ICP base pressure p. In the experiments, a simulated patient is designated as a virtual subject that has a specific value of V.

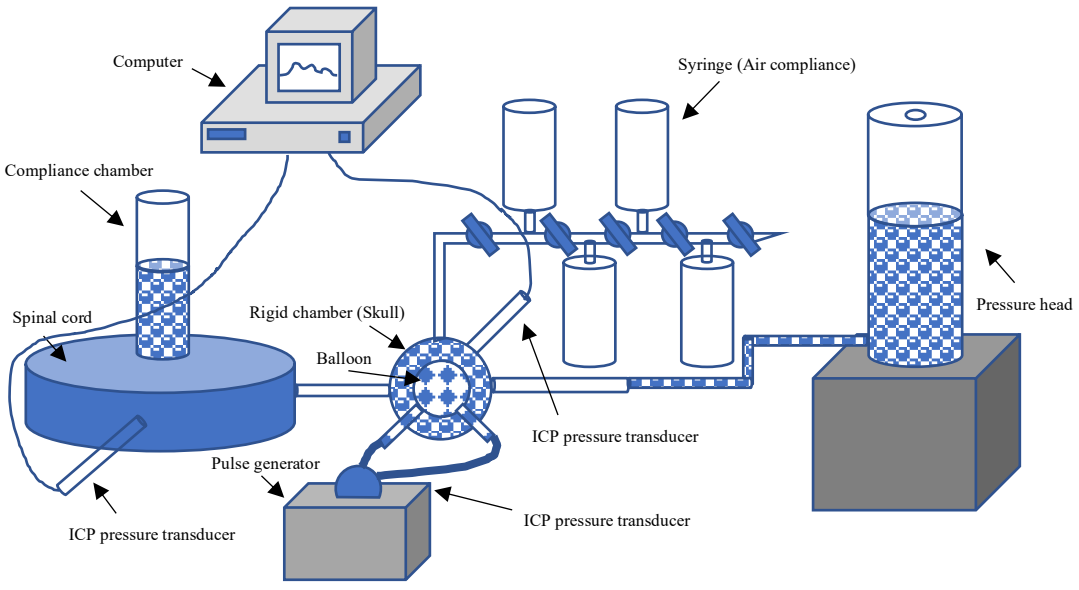

Figure 3.3: Schematic of ICP simulation platform.

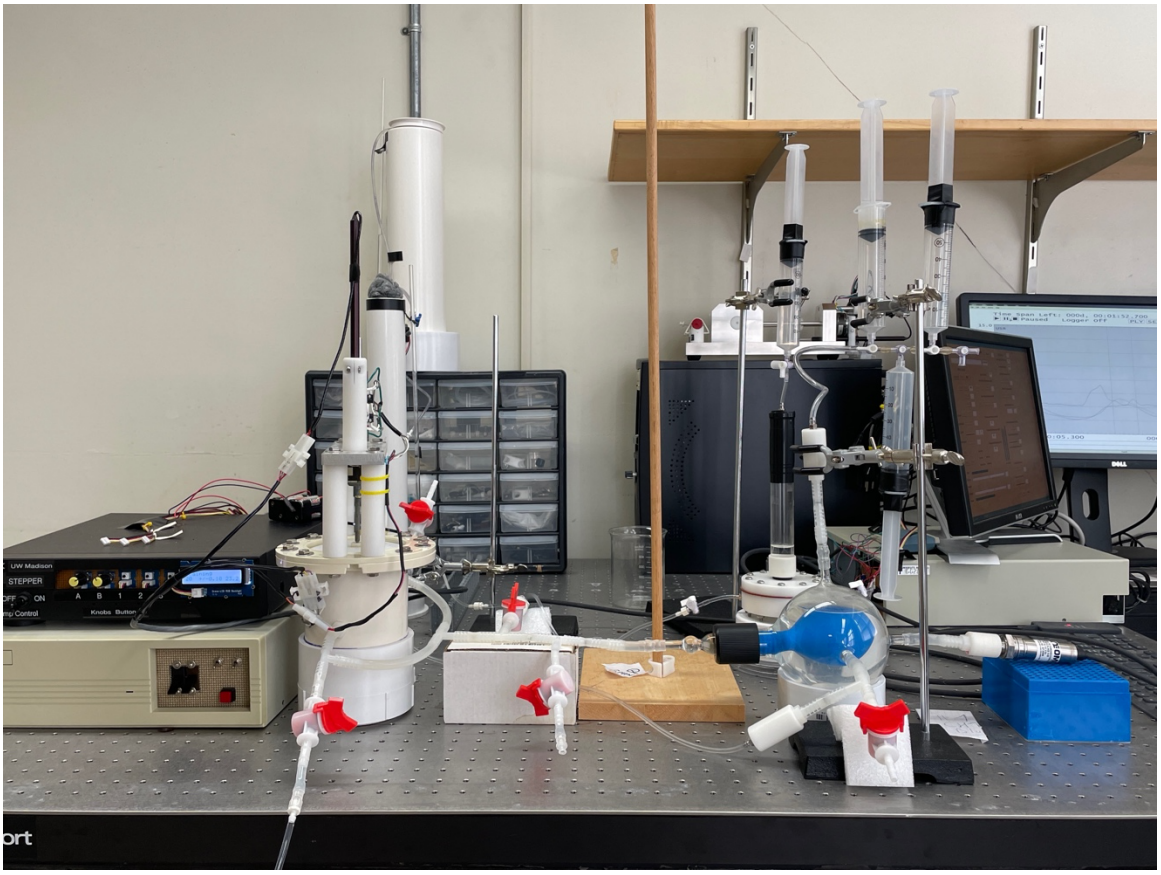

Figure 3.4: ICP simulation platform.

3.5 Experiments settings

Referring to Fig. 3.3, an experiment is performed by setting the air compliance syringe to a specific volume, the ICP pressure head to exert a specific ICP base pressure, and the pulse generator to deliver a sequence pressure pulses periodically at a specific pulsation rate for over 1 minute. This yields a sequence of periodic ICP waveforms recorded by the TracerDaq data logger.

Different combinations of the three factors described above, namely, the air compliance syringe volume, the ICP base pressure, and the cardiac heart rate are chosen to perform various experiments. Specifically,

- 18 different syringe air compliance volumes ranging from 10 ml to 180 ml in increment of 10 ml are chosen. Each of these 18 volumes is designed as a virtual patient. Hence, each patient has a specific value of V, and may have different compliance values depending on the value of p and other factors.
- 7 Base ICP pressures ranging from 5 to 35 cmH_2O in increment of 5 cmH_2O are used.
- 8 Pulsation rates (simulated pulse rate) ranging from 50 to ~120 beats per minute in increment of 100ms of one heartbeat cycle are used.

Each simulated patient would have one specific brain condition. We simulated different patient conditions based on base pressures and pulsation rate. Since not all combinations of these conditions are practical, in total we conducted experiments with ~56 combinations of these two parameters for each of the 18 simulated patients. For each measurement, I measured the volume of the fluid out of the catheter. With the pressure difference between the base pressure and peak pressure, we can calculate the detailed compliance value using equation (3.7). Besides, I performed the simulation for 4 patients gradually adjusting base pressure in one measurement to capture the subtle change between P_1 and P_2. More details for total 22 patients are included in the appendix.

Since continuous measurement prevents manual compliance assessment, we opted to use estimated compliance based on equation (3.7) for these four patients. Prior to each measurement, we injected 5 ml of fluid into the rigid chamber. The pressures before and after the injection were measured. Using equation (3.6), we obtained the pressure-volume index, which was then applied in equation (3.7) to determine the compliance.

For the first 18 patients, based on each set of parameters (compliance, base pressure and pulsation rate), the simulation platform will generate simulated cardiac pulses for 1 min and the corresponding ICP waveform will be recorded in real time using TracerDaq (Figure 3.6). In total, there are 1008 records of ICP waveform for further analysis.

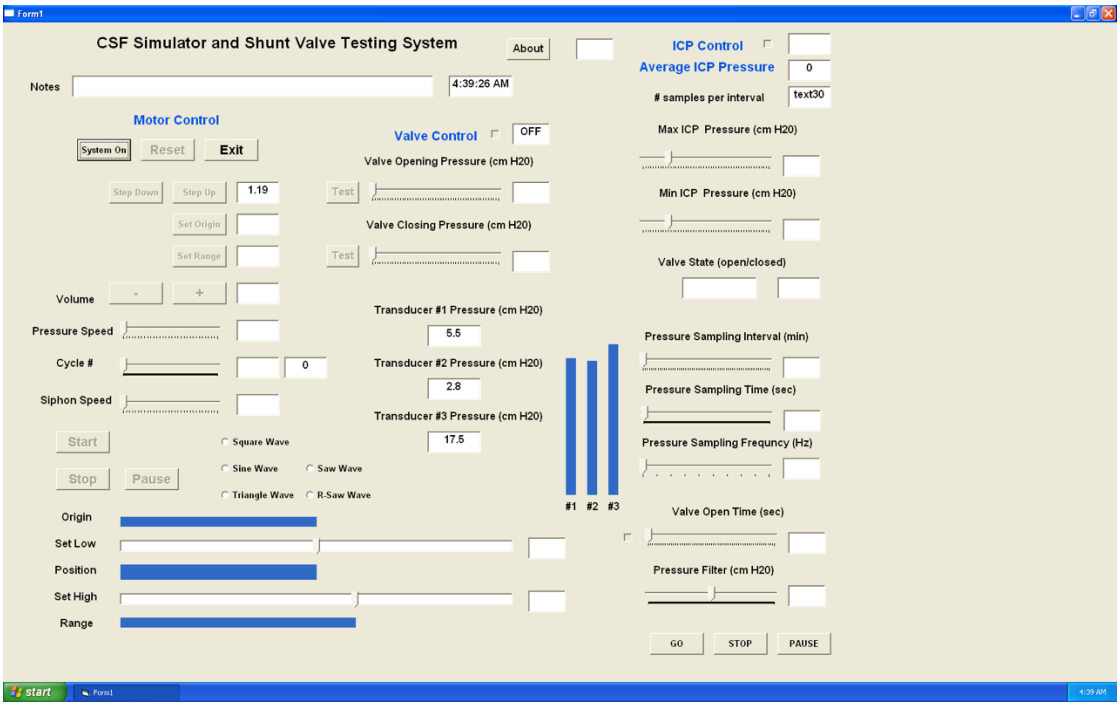

Figure 3.5: ICP monitoring software interface developed by Prof. Luzzio.

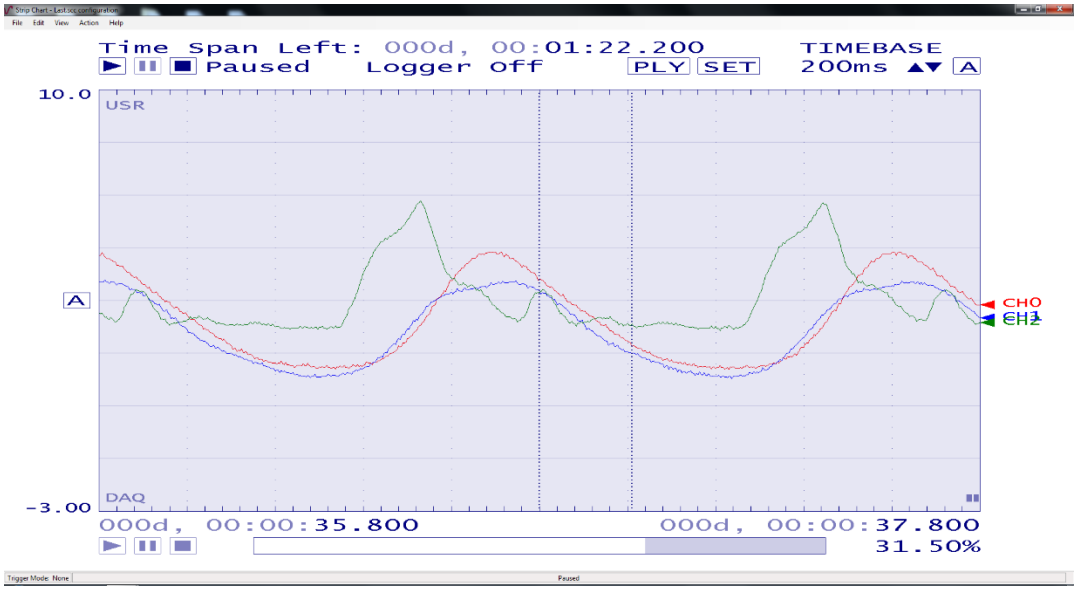

Figure 3.6: TracerDAQ software interface to monitor and capture the pressures from our ICP simulation platform.

3.6 Simulation results

Since the generated ICP waveforms are periodic, it can be characterized by the waveform over one cardiac cycle. In all, 1008 sets of ICP waveforms corresponding to 18 simulated patients and ~800 ICP waveforms corresponding to 4 simulated patients.

Four simulated ICP waveforms from different patients are illustrated in Figure 3.7. These waveforms are taken from four patient with the same base pressure (15mmHg) and pulsation rate (~60 bests per minute). These patients have different brain conditions. Patient A, B, C, D's brain conditions are 10 ml, 60 ml, 120 ml, 180 ml respectively. We observed that the morphologies of these ICP waveforms are quite different. Specifically, as the compliance level decreases, the peak P2 becomes more prominent, and its magnitude gradually increases and exceeds that of P1.

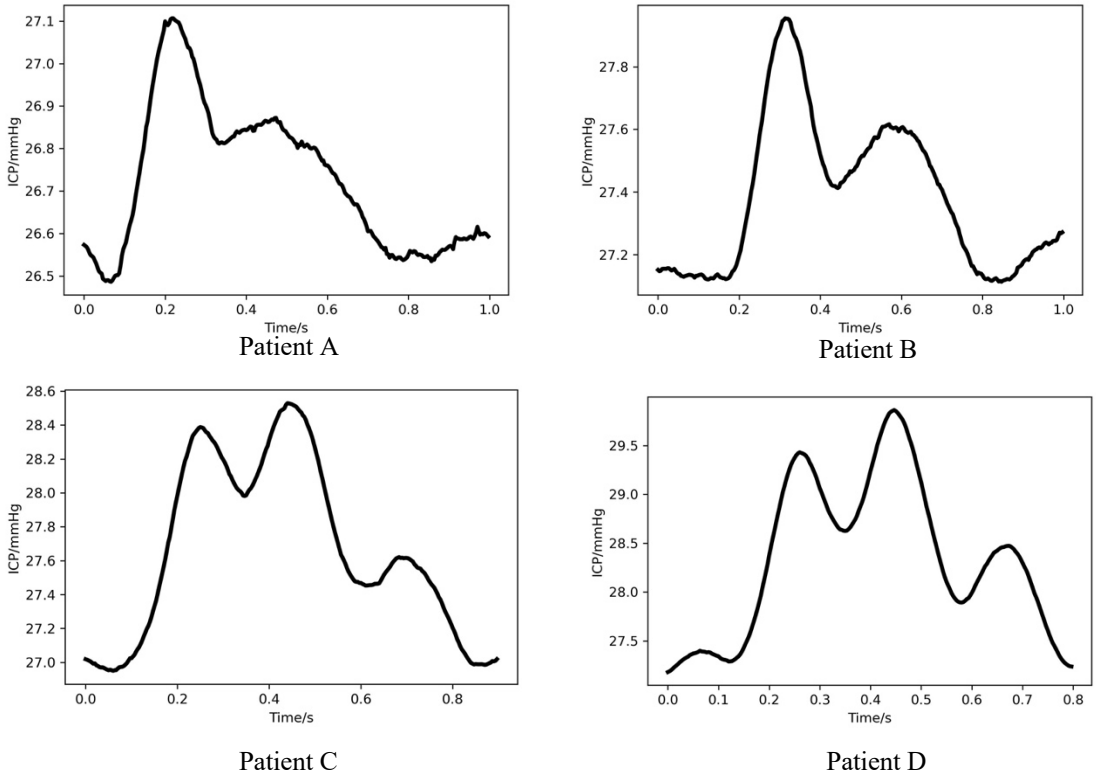

Figure 3.7: Simulated ICP waveforms of different patients at same base pressure and pulsation rate.

In Figure 3.8, the ICP waveforms from one patient with base pressure increasing from 15 cmH_2O to 35 cmH_2O are plotted. With base pressure increasing, the brain compliance keeps decreasing. As the compliance decreasing, the corresponding p2/p1 ratios increase.

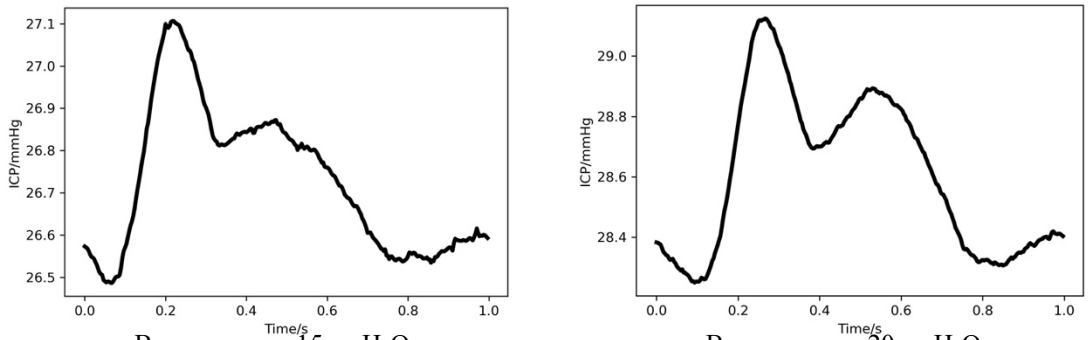

Base pressure: 15 cmH_2O Base pressure: 20 cmH_2O

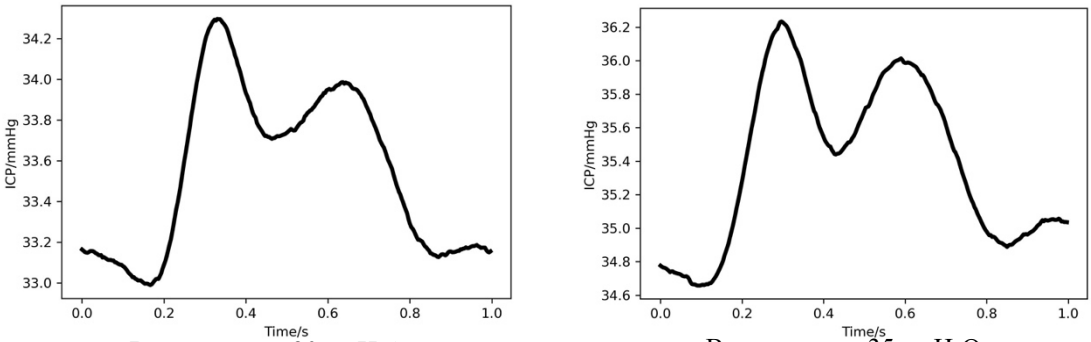

Base pressure: 30 cmH_2O Base pressure: 35 cmH_2O

Figure 3.8: Simulated ICP waveforms of one patient under increasing base pressures.

In Figure 3.9, the impacts of increasing heartbeat rate on the ICP waveforms are illustrated. In this figure, the heartbeat rates vary from 45 to 118 bpm. While the ICP morphologies also moderately change with different heartbeat rates, there does not seem to be a clear trend in terms of the relative peak values of P1 and P2 (Figure 3.10).

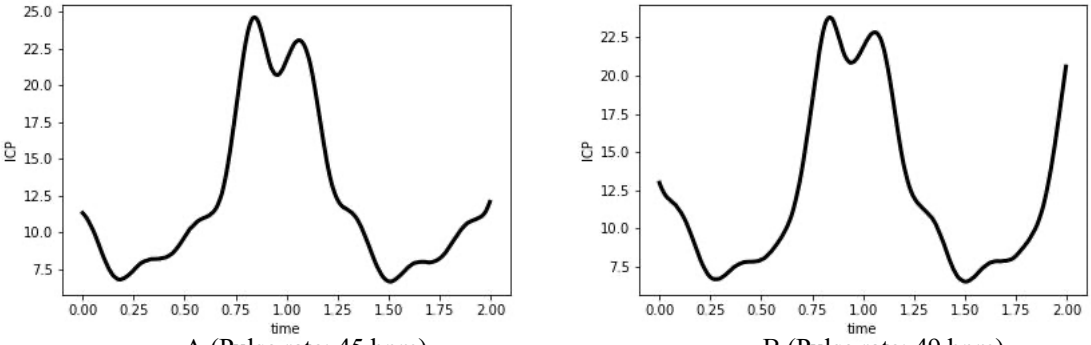

A (Pulse rate: 45 bpm) B (Pulse rate: 49 bpm)

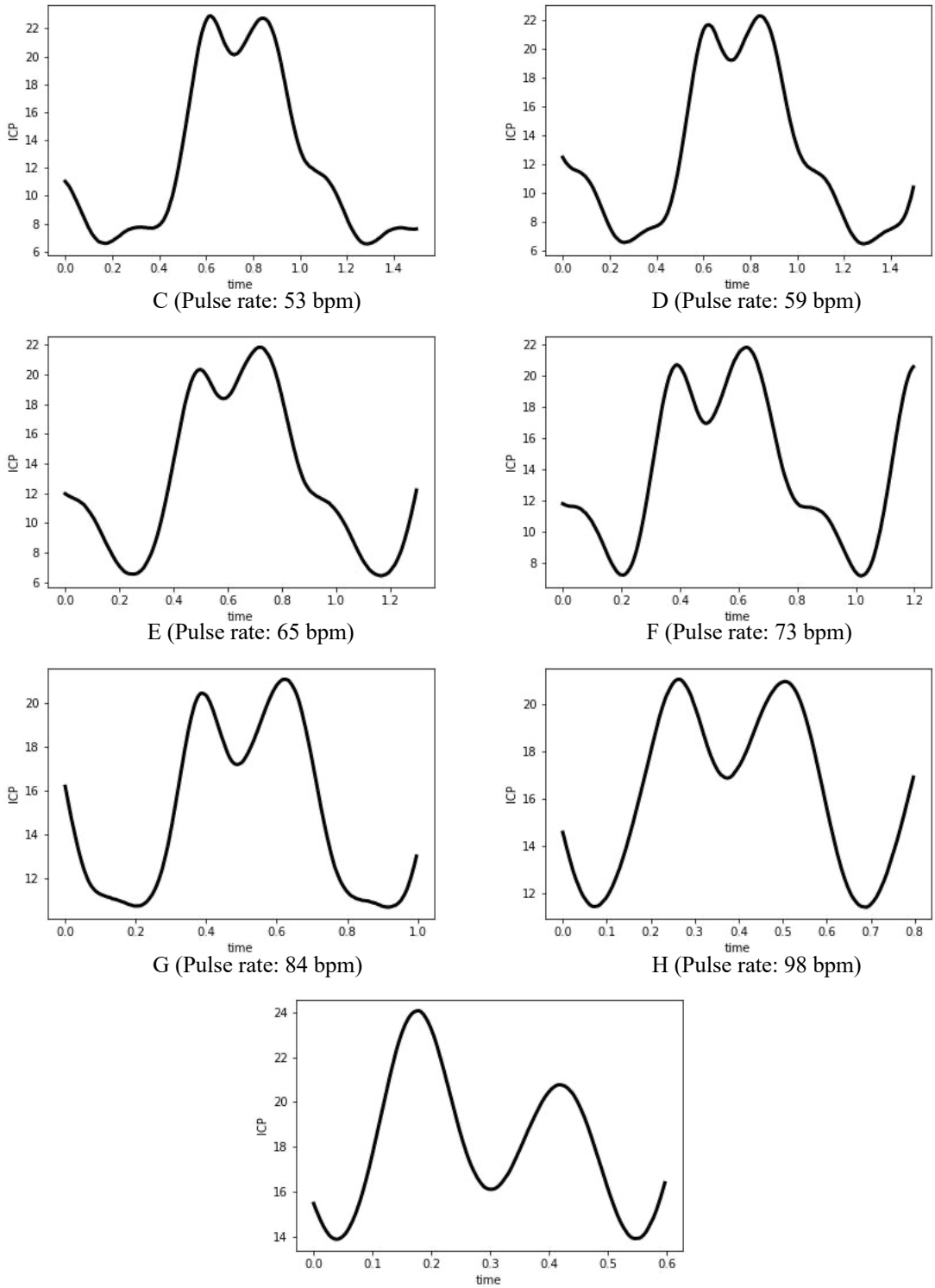

C (Pulse rate: 53 bpm)

D (Pulse rate: 59 bpm)

E (Pulse rate: 65 bpm)

F (Pulse rate: 73 bpm)

G (Pulse rate: 84 bpm)

H (Pulse rate: 98 bpm)

I (Pulse rate: 118 bpm)

Figure 3.9: One simulated patient's ICP waveforms with different pulse rates.

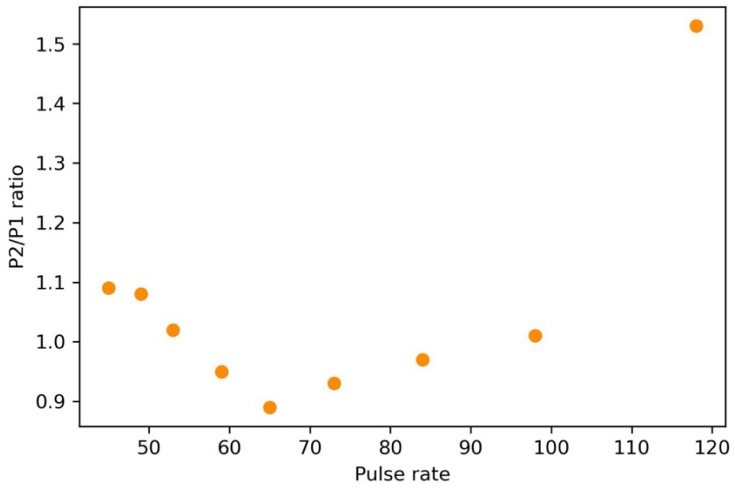

Figure 3.10: A scatter plot of P2/P1 ratio versus heartbeat rate

For these ICP waveforms, we can see distinguishable P1 and P2 peaks without any issue. However, for some cases, we observed that P1 and P2 are not clear so ICP waveforms would be excluded.

3.7 ICP-based compliance estimation

An embedded ICP sensor provides frequent reading of a patient's ICP waveform overtime. In this section, we discuss new methods that promise indirect estimation of the patient's brain compliance based on features extracted from the ICP waveform over a cardiac cycle.

3.7.1 Compliance estimation based on P2/P1 ratio

From the experiment results reported in section 3.6, it is observed that the relative magnitudes of the P1 and P2 peaks of the ICP waveform are correlated to the corresponding compliance values. To be more exact, the P2/P1 ratio seems to be correlated to the compliance levels, which also comply with current clinical observations. For the first 18 simulated patients, under the same pulsation frequency, there are only 5-7 samples with difference base pressure. These samples are

too sparse for analysis based on P2/P1 ratio. Besides some of these ICP waveforms, P1 and P2 are not clear. Thus, we only included patients from #19 to #22 into this analysis.

In Figure 3.11, a scatter plot shows 269 compliance values and corresponding P2/P1 ratios measured from the ICP waveforms recorded in the experiments are plotted as orange dots. Distorted ICP waveform or unidentifiable P1 and P2 were excluded from this analysis. We fit these orange-colored dots to an exponential model:

$$C(Compliance) = a * e^{(-b*\frac{P_2}{P_1})} \tag{3.8}$$

In equation (3.8), P_1 is the pressure of Peak 1 and P_2 is the pressure of Peak 2, *a* and *b* respectively are the parameters for the exponential fit. We will discuss the advantages of this exponential curve fitting function in the section on sensor drift. To estimate the coefficients *a* and *b*, one applies logarithm on both sides of equation (3.8):

$$Log(C) = Log(a) - b\frac{P_2}{P_1}$$

Linear regression estimates the value of Log(a) and b by performing a linear least square fit of $Log(C)$ against P_2/P_1. We partition the data points in Figure 3.11 into a training set and a testing set. The linear least square fitting results are evaluated based on R-square values. The R-squared value for the model is R2 = 0.86.

Substituting these estimated parameters into equation (3.8), patient #22 has

$$C = 2.66 * e^{(-3.3*\frac{P_2}{P_1})}$$

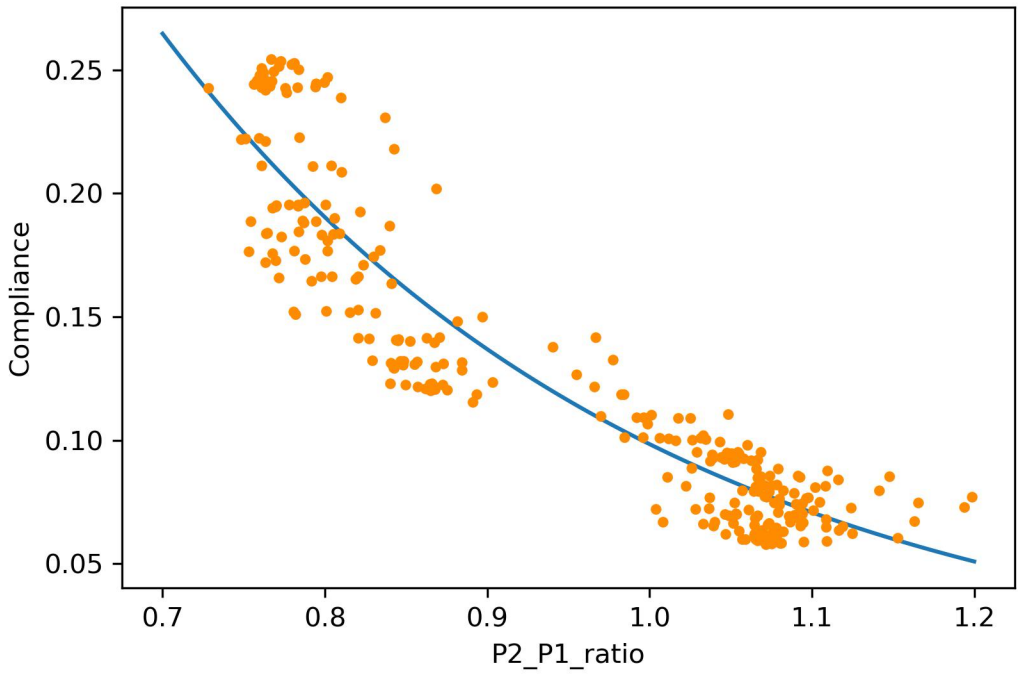

Figure 3.11: A scatter plot of the compliance versus P2/P1 ratio using experiment measurements (orange dots) and the exponential curve (blue line) obtained by fitting these data points.

Patient #	a	b	R-squared
19	4.510	-2.622	0.835
20	1.700	-2.053	0.876
21	158.207	-6.131	0.845
22	2.660	-3.297	0.860

Table 3.1: Exponential models of 4 patients.

In Table 3.1, 4 exponential models are developed from the ICP readings of 4 simulated patients to predict the compliance values using the P2/P1 ratio. Other patients fitting results are included in the appendix.

3.7.2 Compliance estimation based on area under curve in a cardiac cycle

As reported in the experimental results, we found some patients having poor P1 and P2 waves. We also found the same case in clinic monitoring (Figure 3.12). In this circumstance, the P2/P1 ratio does not work well. So, we evaluated the area under the curve method as another solution to estimate intracranial compliance.

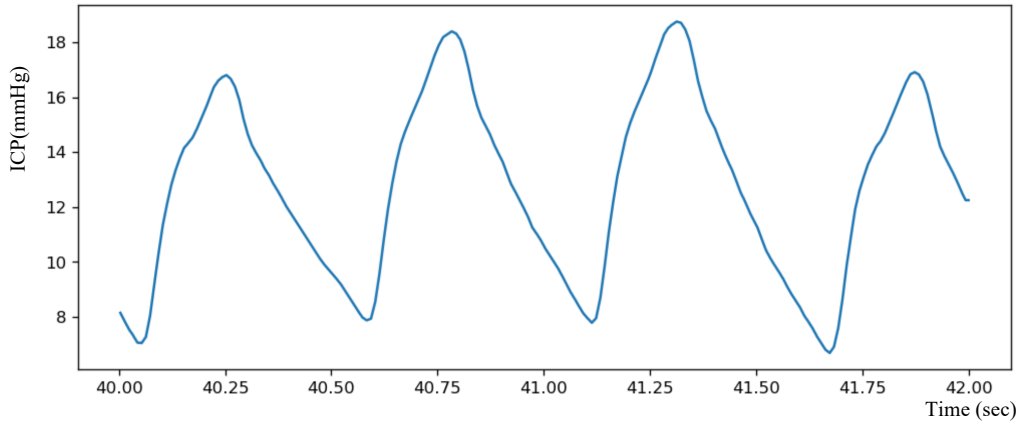

Figure 3.12: One clinical hydrocephalus patient's ICP waveform.

To evaluate the relationship between compliance and area under curve & ICP baseline pressure, we can apply the multiple linear regression model:

$$C\ (Compliance) = a + \ b * AUC + c * ICP_{base} \tag{3.9}$$

We do the curve fitting using linear regression for all the patients. Using our measured data, the curve fitting results are significantly correlative. We can see from Figure 3.13; the fitting result yields an R-squared of 0.999. However, for each patient, we have a very limited number of samples. We can optimize this model to estimate one patient's compliance as a function of their ICP.

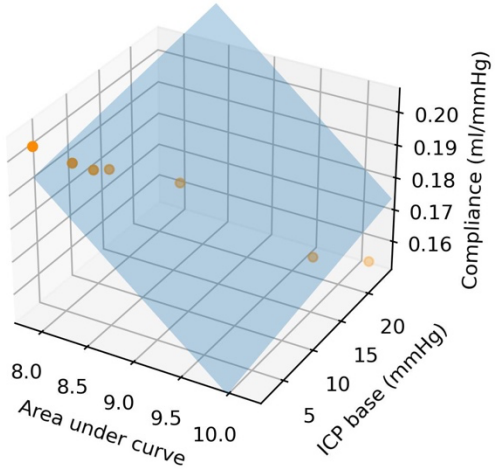

Figure 3.13: One patient's fitting result in 3D space.

Patient #	a	b	c	R-squared
1	0.29346	-0.01110	-0.00118	0.999
2	0.29358	-0.01095	-0.00109	0.996
3	0.38654	-0.02357	0.00037	0.992
4	0.34509	-0.01730	-0.00044	0.995
5	0.37412	-0.02124	0.00011	1.000
6	0.33495	-0.01422	-0.00115	1.000
7	0.40903	-0.02757	0.00103	0.990
8	0.25257	-0.01046	0.00032	0.979
9	0.22519	-0.00752	-0.00026	0.973
10	0.26103	-0.01055	-0.00010	0.988
11	0.26099	-0.01054	-0.00014	0.973
12	0.28712	-0.01300	0.00005	0.988
13	0.27424	-0.01102	-0.00042	0.989
14	0.27699	-0.01268	0.00053	0.993
15	0.59906	-0.04553	0.00554	0.988
16	0.23153	-0.00773	-0.00048	0.983
17	0.29886	-0.01489	0.00051	0.988
18	0.37284	-0.02438	0.00209	0.991

Table 3.2: Multiple linear regression models of 18 patients.

3.7.3 Optimized compliance estimation based on area under curve

In Table 3.2, 18 linear models are developed from the ICP readings of 18 simulated patients to predict the compliance values using the AUC (area under curve) and the ICP baseline pressure. While the models are different for different patients, they seem to be correlated with each other. We may treat the coefficients (*a, b, c*) in each row in Table 3.2 as a 3D point, then as shown in Figure 3.14, viewing from a specific viewpoint, one may see that these points roughly form a straight line in the 3D parameter space. This observation implies that although different patients may have different models, these models may be correlated. In this subsection, we explore this correlation relation and its implications on compliance value monitoring.

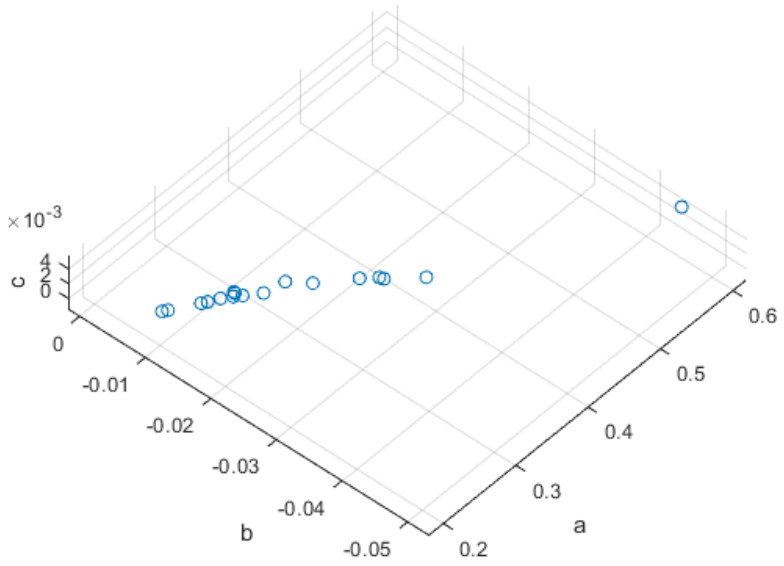

Figure 3.14: The coefficients of the 18 models shown in Table 3.2 approximately form a straight line in the coefficient space (*a, b, c*).

The correlations among the model coefficients of the 18 patients in Figure 3.14 allows one to derive a more efficient representation of such a model. Instead of 18 sets of distinct parameter vectors (*a*, *b*, *c*) for 18 patients, we can derive a formula such that the models of different patients would be characterized by a single parameter. Note that in Figure 3.14, if the underlying straight line is known, these patients' models would differ only by their corresponding

coordinates on this line. For all the points (model parameters) corresponding to 18 different patients to lie on a straight line, a matrix whose rows containing model coefficients of individual patient must have a rank equal to 1. Let **X** be an 18 by 3 matrix formed by entries under the **a**, **b**, and **c** headings in Table 3.2. First, we compute an averaged model by taking the average of each column of the matrix **X**:

$$\bar{a} = 0.3210, \bar{b} = -0.0163, \bar{c} = 0.003$$

Then we subtract these averaged model coefficients from each row of the **X** matrix and denote the result by $\widetilde{\boldsymbol{X}} = \boldsymbol{X} - \mathbf{1} \cdot [\bar{a}\ \ \bar{b}\ \ \bar{c}]$ where **1** is an 18 by 1 column vector with each element equals to 1. Next, we perform singular value deposition on the $\widetilde{\boldsymbol{X}}$ matrix and denote σ_1 to be the largest singular value, and $\mathbf{u}_1$, $\mathbf{v}_1$ respectively to be the left and right singular vector associated with σ_1. Both $\mathbf{u}_1$, and $\mathbf{v}_1$ are uni-norm vectors such that $\boldsymbol{u}_1^T\boldsymbol{u}_1 = 1$ and $\boldsymbol{v}_1^T\boldsymbol{v}_1 = 1$. Then, one may approximate the $\widetilde{\boldsymbol{X}}$ matrix by a rank-1 matrix $\widetilde{\boldsymbol{X}} \approx \sigma_1\boldsymbol{u}_1\boldsymbol{v}_1^T$. As such

$$\boldsymbol{X} = \widetilde{\boldsymbol{X}} + \mathbf{1} \cdot \left[\bar{a}\ \ \bar{b}\ \ \bar{c}\right] \approx \sigma_1\boldsymbol{u}_1\boldsymbol{v}_1^T + \mathbf{1} \cdot [\bar{a}\ \ \bar{b}\ \ \bar{c}] \tag{3.10}$$

Equation (3.10) provides a more efficient way of representing the 18 model parameters (*a*, *b*, *c*) listed in Table 3.2. Denote *a*(*n*), *b*(*n*), and *c*(*n*) to be the model parameters for the n^{th} patient, we have

$$[a(n)\ \ b(n)\ c(n)] \approx u_1(n) \cdot \sigma_1 \cdot [v_1\ \ v_2\ \ v_3] + \left[\bar{a}\ \ \bar{b}\ \ \bar{c}\right] \tag{3.11}$$

Note that in equation (3.11), only one parameter $u_1(n)$ on the right-hand side is dependent on the patient id *n*. Referring to Figure 3.14, equation (3.11) may be interpreted as this: The averaged parameter vector $\left[\bar{a}\ \ \bar{b}\ \ \bar{c}\right]$ is a reference point on the straight line, and

$$\boldsymbol{v}_1^T = [v_1\ \ v_2\ \ v_3] = [0.9945\ \ -0.1041\ \ 0.0140]$$

is a 3D unit-vector pointing the orientation of this straight line. $u_1(n) \cdot \sigma_1$ is the relative distance from the reference point on the line to the n^{th} patient's model parameters. For the 18 patients, σ_1

= 0.3653, and to be exact, we have $\{u_1(n)\cdot \sigma_1, 1 \le n \le 18\}$: [-0.0279 -0.0278 0.0660 0.0241 0.0534 0.0137 0.0888 -0.0686 -0.0962 -0.0602 -0.0602 -0.0340 -0.0470 -0.0441 0.2797 -0.0898 -0.0221 0.0525].

Using equation (3.11), we may deduce the approximated model parameters. Let us use patient #1 as an example. From Table 3.2,

$$[a(1)\ b(1)\ c(1)] = [0.2935\ \ -0.111\ \ -0.0019]$$

Using the right-hand side of equation (3.11), we have

$$u_1(1)\cdot\sigma_1\cdot[v_1\ \ v_2\ \ v_3] + [\bar{a}\ \ \bar{b}\ \ \bar{c}]$$

$$= -0.0279\cdot[0.9945\ \ -0.1041\ \ 0.0140] + [0.3210\ \ -0.0163\ \ 0.003]$$

$$= [0.2932\ \ -0.0134\ \ 0.0026] = [\hat{a}(1)\ \ \hat{b}(1)\ \ \hat{c}(1)]$$

If there is a new patient, not any of the 18 patients, one may use an approximate compliance estimate as: $Compliance = a + b * AUC + c * ICP_{base}$

$$Compliance = \hat{a} + \hat{b} * AUC + \hat{c} * ICP_{base} \tag{3.12}$$

$$= (0.9945 * \alpha + 0.3210) + (-0.1041 * \alpha - 0.0163) * AUC$$

$$+ (0.014 * \alpha - 0.003) * ICP_{base}$$

Here α is the relative distance for this new patient. Suppose that one measurement of compliance value and corresponding AUC, ICP_{base} are available, then one may substitute these measurements into equation (3.12) to estimate the α value as

$$\hat{\alpha} = \frac{Compliance - [\bar{a}\ \ \bar{b}\ \ \bar{c}]\begin{bmatrix}1\\ AUC\\ ICP_{base}\end{bmatrix}}{[v_1\ \ v_2\ \ v_3]\begin{bmatrix}1\\ AUC\\ ICP_{base}\end{bmatrix}} \tag{3.13}$$

For example, initially, during the implanting of the embedded ICP sensor, the patient's compliance value may be measured. Then, by substituting the estimated α value into equation (3.12), the compliance can be estimated given the measured AUC and ICP_{base}.

3.7.4 Apply compliance estimation model to real patients

In subsection 3.7.3, we derived a brain compliance prediction formula using the ICP measurement and compliance values obtained from 18 simulated patients on the ICP simulation platform. By exploiting the similarity of the empirically derived models among different patients, the resulting formula equation (3.12) requires the estimation of a single parameter relative distance α. To estimate the value of α, at least one compliance value measurement is required. However, direct measurements of brain compliance require invasive procedures to be performed which is clinically not feasible.

However, if we assume the parameter α remains unchanged over time, equation (3.12) may be used to gauge the trend of a real patient's compliance over time. Denote subscripts 1 and 2 to be

two time instants when the compliance values of the same patient are to be compared. From equation (3.12), we may compute the difference of the compliance values as

$$\Delta Compliance = Compliance_2 - Compliance_1 \quad (3.14)$$

$$= \left(\hat{a} + \hat{b} * AUC_2 + \hat{c} * ICP_{base,2}\right) - \left(\hat{a} + \hat{b} * AUC_1 + \hat{c} * ICP_{base,1}\right)$$

$$= \hat{b} * (AUC_2 - AUC_1) + \hat{c} * \left(ICP_{base,2} - ICP_{base,1}\right)$$

$$= \hat{b} * \Delta AUC + \hat{c} * \Delta ICP_{base}$$

$$= (-0.1041 * \alpha - 0.0163) * \Delta AUC + (0.014 * \alpha - 0.003)$$

$$* \Delta ICP_{base}$$

$$= (-0.1041 * \Delta AUC + 0.014 * \Delta ICP_{base}) * \alpha + (-0.0163 * \Delta AUC$$

$$- 0.003 * \Delta ICP_{base})$$

For example, for two measurements at different time instants for patient #4:

	Baseline pressure (mmHg)	Area under curve	Compliance (ml/mmHg)
1	15.076	8.405	0.191
2	28.101	10.071	0.159

Table 3.3: Two measurements from one of the 18 patients' data.

From equation (3.14) with Table 3.3, we can get

$\Delta Compliance = Compliance_2 - Compliance_1 = \left(\hat{a} + \hat{b} * AUC_2 + \hat{c} * ICP_{base,2}\right) -$

$\left(\hat{a} + \hat{b} * AUC_1 + \hat{c} * ICP_{base,1}\right) = \hat{b} * (AUC_2 - AUC_1) + \hat{c} * \left(ICP_{base,2} - ICP_{base,1}\right) = \hat{b} *$

$\Delta AUC + \hat{c} * \Delta ICP_{base} = (-0.1041 * \alpha - 0.0163) * \Delta AUC + (0.014 * \alpha - 0.003) *$

$\Delta ICP_{base} = (-0.1041 * \Delta AUC + 0.014 * \Delta ICP_{base}) * \alpha + (-0.0163 * \Delta AUC - 0.003 *$

$\Delta ICP_{base}) = 0.00891 * \alpha - 0.066$

Even though we don't have mature clinic ways to measure compliance so far. However, with our smart shunt, it can drain the fluid out of brain. Based on the volume out of the ventricular

catheters and the ICP pressure change measured by our smart shunt before and after drainage as we described in section 3.3.1, we can get the compliance. With this, we can get the α value. In this manner, we can assess the trend of compliance changes and determine if a patient is experiencing low compliance, potentially requiring emergency intervention.

3.7.5 Potential benefit using P2/P1 ratio for compliance estimation

Capacitive pressure sensors are employed for monitoring ICP pressure and detecting intracranial hypertension. However, due to their flexible polyimide substrates, capacitance value drift can be a drawback during cyclic measurements. Our pressure sensor is based on MEMS capacitive technology, which offers ultra-low noise and minimal power consumption. Capacitive sensors consist of two parallel, electrically isolated conductive plates (Figure 3.15). The bottom plate remains fixed, while the top plate is sensitive to pressure changes. When pressure is applied, the membrane bends, generating a capacitance difference Δ. This change in capacitance is then converted into an electrical signal that can be read by a microcontroller.

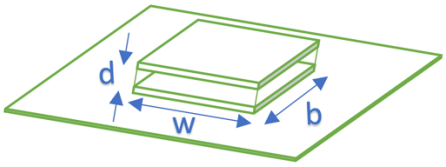

Figure 3.15: Structure of a capacitive sensor.

The capacitance I, measured in Farads (F) of a simple planar capacitor is given by equation (3.15):

$$C = \frac{\varepsilon A}{d} = \frac{\varepsilon_r \varepsilon_0 bw}{d} \tag{3.15}$$

Where:

Width of conductor plate (w) (mm)

Depth of conductor plate (b) (mm)

Area of the plates (A) (mm2)

Displacement between parallel plates (d) (mm)

Permittivity of dielectric(e) (Fm^{-1})

Permittivity of free space (e_0) ($8.85*10^{-12}\ Fm^{-1}$)

Relative permittivity (e_r)

When considering the sensor accuracy and long-term drift, it would drift gradually. For the state of art pressure sensor, the drift can be ±40 Pa/year, which is ±0.3mmHg. There are two types of drifting: zero drift and span drift, Figure 3.16.

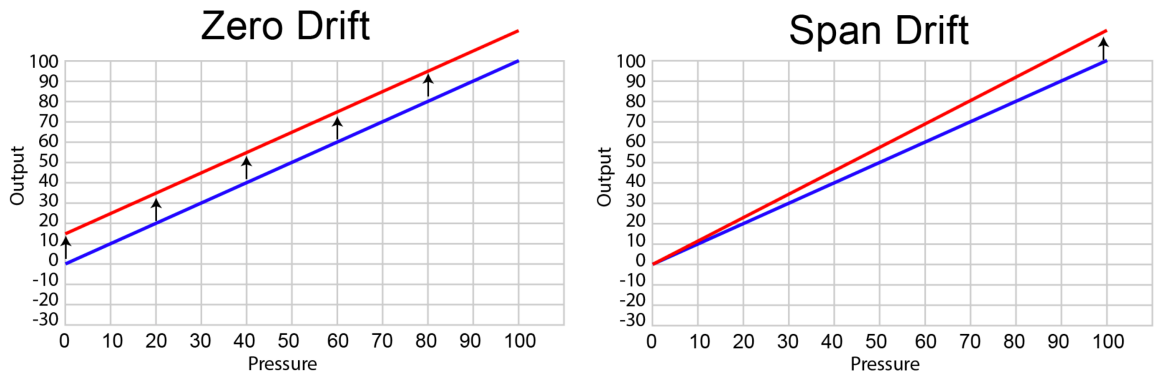

Figure 3.16: Two types of sensors drifting over long-term use.

After the long-term use, the drifted pressure would be

$$P_{drifted} = P_{accurate} * \left(1 + ratio_{drifted}\right) + P_{drifted\ baseline} \quad (3.16)$$

As we can see from the following Table 3.4, when we use first model to estimate the brain compliance based on the P2/P1 ratio, it is immune to the effect of sensor drift. One thing noted

here is when we calculate the P2/P1 ratio, we would subtract the baseline pressure for both. We can still get accurate brain compliance after long term use.

	No sensor drifting	Sensor drifting
Average ICP pressure	P_{mean}	$P_{mean} * (1 + ratio) + P_{drifted\_baseline}$
P1	P_1	$P_1 * (1 + ratio) + P_{drifted\_baseline}$
P2	P_2	$P_2 * (1 + ratio) + P_{drifted\_baseline}$
P2 /P1	$(P_2 - P_{mean})/(P_1 - P_{mean})$	$(P_2 - P_{mean})/(P_1 - P_{mean})$

Table 3.4: P2/P1 ratio comparison before and after sensor drift.

When we use second model to estimate the brain compliance, we would get equation (3.17).

$$Compliance = a + b * AUC\left(1 + ratio_{drifted}\right) + c * (ICP_{base} + P_{drifted\ baseline}) \quad (3.17)$$

We can compare these two results and see the sensor itself is drifted or not in the long term.

3.8 Conclusion

This study is the first to continuously measure brain compliance using our ICP simulation platform. Leveraging the platform, I proposed two distinct models for estimating patient compliance: one based on the P2/P1 ratio and the other on the area under the curve and baseline pressure. For ICP waveforms with identifiable P1, P2, and P3 peaks, we prefer the P2/P1 ratio-based compliance estimation method, as it can mitigate the impact of sensor drift over time. For ICP waveforms without discernible P1, P2, P3 peaks, a multilinear regression model based on baseline ICP and area under the curve (AUC) can be employed to estimate compliance for each patient. Experimental results indicate that although different patients may have distinct models, there may be correlations between these models. This insight allows us to investigate these correlations and their implications for compliance value monitoring.

To further optimize this approach, we can analyze all patients' ICP waveform information and extract essential features through singular value decomposition. These methods, based on in vitro

studies, demonstrate significant potential in assisting doctors in quantifying compliance through ICP devices.

3.9 Acknowledgement

We would like to express our sincere gratitude to Professor Christopher Luzzio, Dept, Neurology, UW-Madison, and his team for the collaboration in developing the ICP simulation platform.

3.10 Appendix

Experiment #	Brain condition(ml)	Base pressure (mmH_2O)	Pulsation frequency (beats per minute)
1 (Dec 10, 2021)	60	23.6, 29, 30	60
2 (Feb 12, 2022)	180	20	60
3 (Feb 18, 2022)	10, 60, 120, 180	20	60
4 (Mar 18, 2022)	10, 60, 120, 180, 240	10, 15, 20, 25, 30, 35, 40	60
5 (Mar 23, 2022)	10, 60, 120, 180	15, 20, 25, 30	60
6 (May 3, 2022)	10, 60, 120, 180	20, 25, 30, 35, 40	10, 30, 60, 90, 120
7 (May 7, 2022)	10, 15, 20, 25, 30, 35	15, 20, 25, 30, 35, 40	45, 49, 53, 60, 65, 73, 84, 98, 118
8 (May 22, 2022)	20, 40, 60, 70	15-40(Continuously)	60
9 (May 26, 2022)	10	15-40(Continuously)	60
10 (Sep 28, 2022)	10, 20, 30, 40, 50, 60	15, 20, 25, 30, 35, 40, 15-40(Continuously)	45, 49, 53, 60, 65, 73, 84, 98, 118

Table 3.5: Experimental protocol when conducting experiments. The 18 patients are from experiment #10. The following 4 patients are from experiment #8.

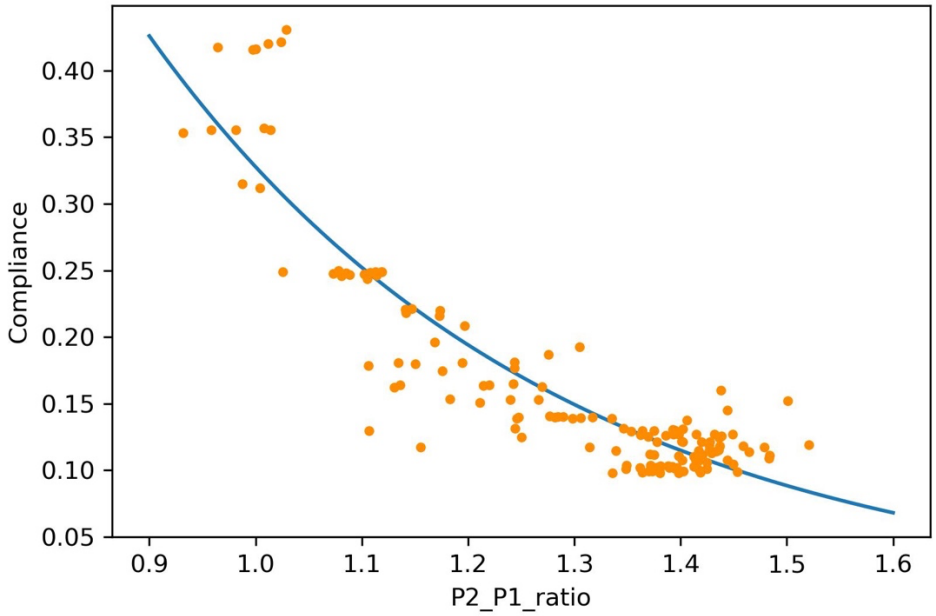

Figure 3.17: A scatter plot of the compliance versus P2/P1 ratio using experiment measurements (orange dots) and the exponential curve (blue line) obtained by fitting these data points.(Patient #19)

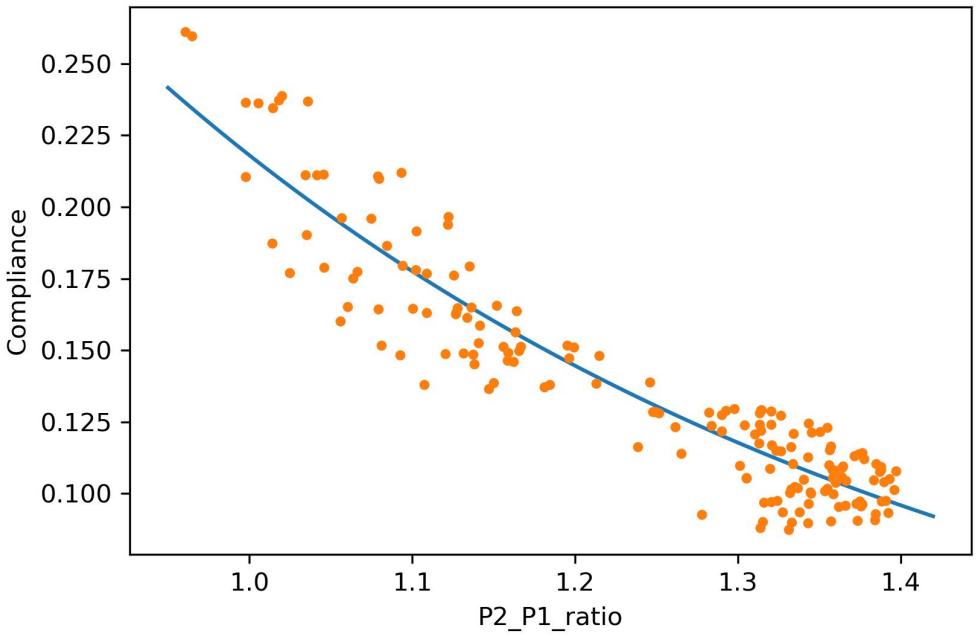

Figure 3.18: A scatter plot of the compliance versus P2/P1 ratio using experiment measurements (orange dots) and the exponential curve (blue line) obtained by fitting these data points.(Patient #20)

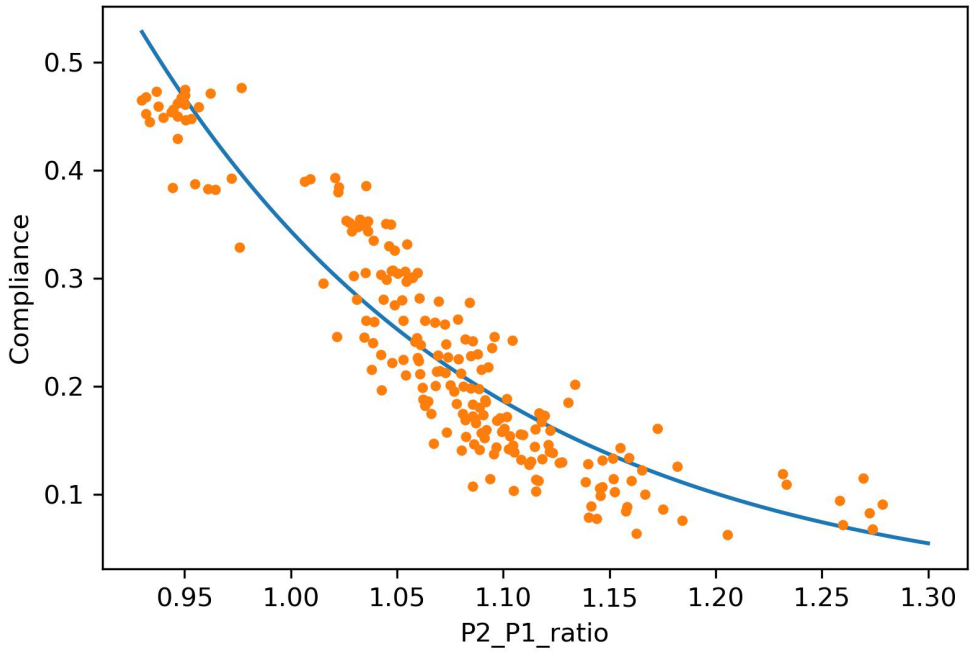

Figure 3.19: A scatter plot of the compliance versus P2/P1 ratio using experiment measurements (orange dots) and the exponential curve (blue line) obtained by fitting these data points.(Patient #21)

Chapter 4: Summary

This dissertation presents two main aspects of my work: 1) the development of a smart shunt device, and 2) brain compliance estimation based on ICP waveform information. For the smart shunt, I designed and constructed a demonstration prototype, which includes a sensor reader circuit, valve driver circuit, and control circuit. Our smart shunt can read ICP pressure from our custom ICP pressure sensor and generate high voltages (±100V) to open or close our piezo-actuated shunt valve. With a novel control algorithm, the smart shunt can open the valve when the average ICP value exceeds the upper threshold and instantly close the valve when the ICP instant value falls below the lower threshold, preventing over-drainage. Due to its low power consumption, our device can operate continuously for over 2.6 days when fully charged. Additionally, I developed a brain compliance simulation platform to model ICP waveforms, simulating over 18 patients' ICP waveform data for brain compliance analysis. Based on the measurement results, I proposed two methods for estimating brain compliance: through the P2/P1 ratio or the combination of the area under the curve and baseline pressure. We also observed that although different patients have distinct models, these models can be correlated, allowing us to explore this relationship and its implications on compliance value monitoring. The full prototype of the implantable smart shunt, comprising a pressure sensor to monitor intracranial pressure and an algorithm-controlled valve, has been successfully designed and implemented.

Future work can involve further refining the brain compliance simulation platform to simulate brain behavior under a wider range of conditions and evaluate the accuracy of compliance

estimation. By enhancing the brain compliance simulation platform, we can develop a deeper understanding of the interplay between mechanical forces exerted on the brain and its subsequent reactions, which can assist in the advancement of novel medical treatments and devices. As discussed in Chapter 3, CSF flow is a crucial factor for our shunt as it pertains to the volume of CSF exiting the ventricle. Presently, no clinical methods exist for in situ or in vivo measurement of CSF flow. We could work on developing an implantable CSF-flow sensor capable of providing reliable flow recordings, such as the implantable blood-flow sensor (Vennemann et al. in 2020).

References

Akar, O., Akin, T., & Najafi, K. (2001). A wireless batch sealed absolute capacitive pressure sensor. Sensors and Actuators A: Physical, 95(1), 29-38.

Allocca J A 1980 Method and apparatus for noninvasive monitoring of intracranial pressure U.S. Patent 4,204,547

Alperin N J, Lee S H, Loth F, Raksin P B and Lichtor T 2000 MR-Intracranial Pressure (ICP): A method to measure intracranial elastance and pressure noninvasively by means of MR Imaging: baboon and human study 1 Radiology 217 877–85

Alperin N, Hushek S G, Lee S H, Sivaramakrishnan A and Lichtor T 2005 MRI study of cerebral blood flow and CSF flow dynamics in an upright posture: the effect of posture on the intracranial compliance and pressure In Kirkness C J et al. (eds) Intracranial Pressure and Brain Monitoring XII (Springer; Vienna) pp. 177–81

Anderson R C, Kan P, Klimo P, Brockmeyer D L, Walker M L and Kestle J R 2004 Complications of intracranial pressure monitoring in children with head trauma J. Neurosurg.: Pediatrics 101 53-8

Anonymous 2000 The Brain Trauma Foundation. The American Association of Neurological Surgeons. The Joint Section on Neurotrauma and Critical Care. Recommendations for intracranial pressure monitoring technology J. Neurotraum. 17 497–506

Antes S, Tschan C A, Kunze G, Ewert L, Zimmer A, Halfmann A and Oertel J 2014 Clinical and radiological findings in long-term intracranial pressure monitoring. Acta Neurochir. 156 1009–19

Asiedu D P, Lee K J, Mills G and Kaufmann E E 2014 A Review review of non-invasive methods of monitoring intracranial pressure J. Neurolog. Res. 4 1–6

Avan P, Büki B, Lemaire J J, Dordain M and Chazal J 1996 Otoacoustic emissions: a new tool for monitoring intracranial pressure InIntracranial and intralabyrinthine fluids (Springer; Berlin Heidelberg) 165–73

Bauer D F, Razdan S N, Bartolucci A A and Markert J M 2011 Meta-analysis of hemorrhagic complications from ventriculostomy placement by neurosurgeons Neurosurgery 69 255–60

Baurmann M 1925 Über die entstehung und klinische bedeutung des netzhautvenenpulses Dtsch. Ophthalmol. Ges. 45 53–9

Beer R, Lackner P, Pfausler B and Schmutzhard E 2008 Nosocomial ventriculitis and meningitis in neurocritical care patients J. Neurol. 255 1617–24

Bekar A, Doğan Ş, Abaş F, Caner B, Korfalı G, Kocaeli H, Yılmazlar S and Korfalı E 2009 Risk factors and complications of intracranial pressure monitoring with a fiberoptic device J. Clin. Neurosci. 16 236–40

Bermans Iskandar,Joshua Medow,Christopher Luzzio,John Webster,Mehdi Shokoueinejad Maragheh,Fa Wang,Xuan Zhang,CEREBROSPINAL FLUID SHUNT VALVE SYSTEM

Xuan Zhang, Joshua E. Medow, Bermans J. Iskandar, Fa Wang, Mehdi Shokoueinejad, Joyce Koueik, and John G. Webster. Invasive and noninvasive means of measuring intracranial pressure: A review May.2017 Physiol. Meas.

Webster JG, Iskandar B, Medow J, Luzzio C, Zhang X, Guan C, Yang Z. Intracranial Pressure Sensor and Valve to Control Hydrocephalus. Annu Int Conf IEEE Eng Med Biol Soc. 2018 Jul;2018:1-7. doi: 10.1109/EMBC.2018.8512916. PMID: 30440275.

Berlin T, Murray-Krezan C and Yonas H 2015 Comparison of parenchymal and ventricular intracranial pressure readings utilizing a novel multi-parameter intracranial access system. SpringerPlus 4 10

Bershad E M, Urfy M Z, Pechacek A, McGrath M, Calvillo E, Horton N J and Voss S E 2014 Intracranial pressure modulates distortion product otoacoustic emissions: A proof-of-principle study Neurosurgery 75 445–55

Bhatia A and Gupta A K 2007 Neuromonitoring in the intensive care unit. I. Intracranial pressure and cerebral blood flow monitoring Intens. Care Med. 33 1263–71

Binz D D, Toussaint III L G, and Friedman J A 2009 Hemorrhagic complications of ventriculostomy placement: a meta-analysis Neurocrit. Care 10 253–6

Borchert M S and Lambert J L 1998 Non-invasive measurement of intracranial pressure WO Patent 98034536

Borchert M S and Lambert J L 2000 Non-invasive method of measuring cerebral spinal fluid pressure U.S. Patent 6,129,682

Brain T F 2007 Guidelines for the management of severe traumatic brain injury. V. Deep vein thrombosis prophylaxis J. Neurotraum. 24 S32

Bratton S L, Chestnut, R M, Ghajar J, McConnell H F, Harris O A, Hartl R, Manley GT, Nemecek A, Newell DW, Rosenthal G and Schouten J 2006 Guidelines for the management of severe traumatic brain injury. VII. Intracranial pressure monitoring technology J. Neurotraum. 24 S45–54

Bruce B B 2014 Noninvasive assessment of cerebrospinal fluid pressure J. Neuro-Ophthalmol. 34 288–94

Bruder N, N'Zoghe P, Graziani N, Pelissier D, Grisoli F and François G 1995 A comparison of extradural and intraparenchymatous intracranial pressures in head injured patients Intens. Care Med. 21 850–2

Büki B, Giraudet F and Avan P 2009 Non-invasive measurements of intralabyrinthine pressure changes by electrocochleography and otoacoustic emissions Hearing Res. 251 51–9

Butler, J. C., Vigliotti, A. J., Verdi, F. W., & Walsh, S. M. (2002). Wireless, passive, resonant-circuit, inductively coupled, inductive strain sensor. Sensors and Actuators A: Physical, 102(1), 61-66.

Bullock M R and Povlishock J T 2007 Guidelines for the management of severe traumatic brain injury Editor's Commentary J. Neurotraum. 24 Suppl 1:2 p preceding S1.

Chen H, Wang J, Mao S, Dong W and Yang H 2012 A new method of intracranial pressure monitoring by EEG power spectrum analysis Can. J. Neurol. Sci. 39 483–7

Chen L Y, Tee B C K, Chortos A L, Schwartz G, Tse V, Lipomi D J, Wong H S P, McConnell M V and Bao Z 2014 Continuous wireless pressure monitoring and mapping with ultra-small passive sensors for health monitoring and critical care. Nat. Commun. 5 5028

Chen, P. J., Saati, S., Varma, R., Humayun, M. S., & Tai, Y. C. (2010). Wireless intraocular pressure sensing using microfabricated minimally invasive flexible-coiled LC sensor implant. Journal of Microelectromechanical Systems, 19(4), 721-734.

Chitnis, G., Maleki, T., Samuels, B., Cantor, L. B., & Ziaie, B. (2013). A minimally invasive implantable wireless pressure sensor for continuous IOP monitoring. IEEE Transactions on Biomedical Engineering, 60(1), 250-256.

Citerio G, Piper I, Chambers I R, Galli D, Enblad P, Kiening K, Ragauskas A, Sahuquillo J and Gregson B 2008 Multicenter clinical assessment of the raumedic neurovent–P intracranial pressure sensor: a report by the Brainit group Neurosurgery 63 1152–8

Cleveland, W. S., & Loader, C. (1996). Smoothing by local regression: Principles and methods. In Statistical theory and computational aspects of smoothing (pp. 10-49). Physica-Verlag HD.

Collins, Carter C. "Miniature passive pressure transensor for implanting in the eye." IEEE Transactions on Biomedical Engineering 2 (1967): 74-83.

Comsol, COMSOL Multiphysics: Version 4.2: Comsol, 2011.

Coosemans, Johan, Michael Catrysse, and Robert Puers. "A readout circuit for an intra-ocular pressure sensor." Sensors and Actuators A: Physical 110.1 (2004): 432-438.

Czosnyka M and Pickard J D 2004 Monitoring and interpretation of intracranial pressure J. Neurol. Neurosur. Ps. 75 813–21

Czosnyka M, Czosnyka Z and Pickard J D 1996 Laboratory testing of three intracranial pressure microtransducers: technical report Neurosurgery 38 219–24

Dasic D, Hanna S J, Bojanic S and Kerr R C 2006 External ventricular drain infection: the effect of a strict protocol on infection rates and a review of the literature Brit. J. Neurosurg. 20 296–300

Di Ieva A Schmitz E M and Cusimano M D 2013 Analysis of intracranial pressure past, present, and future Neuroscientist 1073858412474845

Du R, Meeker M, Bacchetti P, Larson M D, Holland M C and Manley G T 2005 Evaluation of the portable infrared pupillometer Neurosurgery 57 198–203

Dunn L T 2002 Raised intracranial pressure J. Neurol. Neurosur. Ps. 73 i23–7

Duschek S and Schandry R 2007 Reduced brain perfusion and cognitive performance due to constitutional hypotension. Clin. Auton. Res. 17 69–76

Eide PK 2006 A new method for processing of continuous intracranial pressure signals. Med. Eng. Phys. 28: 579–87

Eide P K 2008 Comparison of simultaneous continuous intracranial pressure (ICP) signals from ICP sensors placed within the brain parenchyma and the epidural space Med. Eng. Phys. 30 34-40

Eide P K and Brean A 2006 Lumbar cerebrospinal fluid pressure waves versus intracranial pressure waves in idiopathic normal pressure hydrocephalus Brit. J. Neurosurg. 20 407–14

Eide P K and Sæhle T 2010 Is ventriculomegaly in idiopathic normal pressure hydrocephalus associated with a transmantle gradient in pulsatile intracranial pressure? Acta Neurochir. 152 989–95

English, J. M., & Allen, M. G. (1999, January). Wireless micromachined ceramic pressure sensors. In Micro Electro Mechanical Systems, 1999. MEMS'99. Twelfth IEEE International Conference on (pp. 511-516). IEEE.

Firsching R, Müller C, Pauli S U, Voellger B, Röhl F W and Behrens-Baumann W 2011 Noninvasive assessment of intracranial pressure with venous ophthalmodynamometry: Clinical article. J. Neurosurg. 115 371–4

Fountas K N, Kapsalaki E Z, Machinis T G, Boev A N, Robinson III J S and Troup E C 2006 Clinical implications of quantitative infrared pupillometry in neurosurgical patients Neurocrit. Care 5 55–60

Fountas K N, Sitkauskas A, Feltes CH, Kapsalaki E Z, Dimopoulos V G, Kassam M, Grigorian A A, Robinson J S and Ragauskas A, 2005 Is non-invasive monitoring of intracranial pressure waveform analysis possible? Preliminary results of a comparative study of non-invasive vs.

invasive intracranial slow-wave waveform analysis monitoring in patients with traumatic brain injury Med Sci. Monit. 11 CR58–63

Fried H I, Nathan B R, Rowe A S, Zabramski J M, Andaluz N, Bhimraj A, Guanci M M, Seder D B and Singh J M 2016 The insertion and management of external ventricular drains: an evidence-based consensus statementNeurocrit. Care 24(1) pp. 61-81

Freimann F B, Sprung C, Chopra S S, Vajkoczy P and Wolf S 2013 Large-scale referencing of the telemetric Neurovent-P-tel intracranial pressure sensor in a porcine model. Pediatr. Neurosurg. 49 29–32

Gaab M R, Heissler H E and Ehrhardt K 1989 Physical characteristics of various methods for measuring ICP Intracranial Pressure VII (Springer; Berlin Heidelberg) pp. 16–21

Gaihede M, Felding J U and Elbrônd O 1995 Biomechanical characteristics of the middle ear system measured by a new method: III: Comparisons with tympanometric measurements Acta oto-laryngol. 115 522–7

Gardner P A, Engh J, Atteberry D and Moossy J J 2009 Hemorrhage rates after external ventricular drain placement: clinical article J. Neurosurg. 110 1021–5

Geeraerts T, Merceron S, Benhamou D, Vigué B and Duranteau J 2008a Noninvasive assessment of intracranial pressure using ocular sonography in neurocritical care patients Crit. Care 12 1–2

Gelabert-Gonzalez M, Ginesta-Galan V, Sernamito-Garcia R, Allut A G, Bandin-Dieguez J and Rumbo R M 2006 The Camino intracranial pressure device in clinical practice. Assessment in a 1000 cases Acta Neurochir. (Wien) 148 435–41

Gevorgian, S., et al. "Application notes-basic parameters of coplanar-strip waveguides on multilayer dielectric/semiconductor substrates, Part 1: high permittivity superstrates." IEEE microwave magazine 4.2 (2003): 60-70.

Ghajar J 1995 Intracranial pressure monitoring techniques New Horiz. 3 395–9

Glick R P, Niebruegge J, Lee S H, Egibor O, Lichtor T and Alperin N 2006 Early experience from the application of a noninvasive magnetic resonance imaging-based measurement of intracranial pressure in hydrocephalus Neurosurgery 59 1052–61

Graham D I, Gennarelli T A, Cooper P R, and Golfinos J G 2000 Pathology of brain damage after head injury. In P R Cooper and J Golfinos (eds) Head injury 4th edn (New York: McGraw-Hill) 133–54

Guild S J, McBryde F D and Malpas S C 2015 Recording of intracranial pressure in conscious rats via telemetry J. Appl. Physiol. 119 576–81

Hanlo P W, Gooskens R H J M, Faber J A J, Peters R J A, Nijhuis A A M, Vandertop W P, Tulleken C A F and Willemse J 1996 Relationship between anterior fontanelle pressure measurements and clinical signs in infantile hydrocephalus Child Nerv. Syst. 12 200–9

Hanlo P W, Peters R J A, Gooskens R H J M, Heethaar R M, Keunen R W M, van Huffelen A C, Tulleken A F, and Willemse J 1995 Monitoring intracranial dynamics by transcranial Doppler—A new Doppler index: Trans systolic time Ultrasound Med. Biol. 21 613–21

Hawthorne C and Piper I 2014 Monitoring of intracranial pressure in patients with traumatic brain injury Front. Neurol. 5 121

Hee M R, Izatt J A, Swanson E A, Huang D, Schuman J S, Lin C P, Puliafito C A and Fujimoto J G 1995 Optical coherence tomography of the human retina Arch. Ophthalmol-chic. 113 325–32

Hoefnagel D, Dammers R, Ter Laak-Poort M P and Avezaat C J J 2008 Risk factors for infections related to external ventricular drainage Acta Neurochirur. 150 209–14

Hong W C, Tu Y K, Chen Y S, Lien L M and Huang S J 2006 Subdural intracranial pressure monitoring in severe head injury: clinical experience with the Codman MicroSensor Surg. Neurol. 66 S8–13

Hori, Hiroyuki, et al. "The thickness of human scalp: normal and bald." Journal of Investigative Dermatology 58.6 (1972): 396-399.

Hydrocephalus Association (2016) http://www.hydroassoc.org/

IEEE Standards Coordinating Committee 28, on Non-Ionizing Radiation Hazards. (1992). IEEE Standard for Safety Levels with Respect to Human Exposure to Radio Frequency Electromagnetic Fields, 3kHz to 300 GHz. Institute of Electrical and Electonics Engineers, Incorporated.

Jacks A S and Miller N R 2003 Spontaneous retinal venous pulsation: aetiology and significance J. Neurol. Neurosur. Ps. 74 7–9

Jonas J B, Pfeil K, Chatzikonstantinou A and Rensch F 2008 Ophthalmodynamometric measurement of central retinal vein pressure as surrogate of intracranial pressure in idiopathic intracranial hypertension Graef. Arch. Clin. Exp. 246 1059–60

Jonas J B, Wang N and Yang D 2012 Retinal vein pulsation is in phase with intracranial pressure and not intraocular pressure Invest. Ophth. Vis. Sci. 53 6045

Jow, Uei-Ming, and Maysam Ghovanloo. "Design and optimization of printed spiral coils for efficient transcutaneous inductive power transmission." IEEE Transactions on biomedical circuits and systems 1.3 (2007): 193-202.

Kang S K, Murphy R K, Hwang S W, Lee S M, Harburg D V, Krueger N A, Shin J, Gamble P, Cheng H, Yu S and Liu Z 2016 Bioresorbable silicon electronic sensors for the brain Nature 530 71–9

Kapadia F N and Jha A N 1996 Simultaneous lumbar and intraventricular manometry to evaluate the role and safety of lumbar puncture in raised intracranial pressure following subarachnoid haemorrhage Brit. J. Neurosurg. 10 585–8

Kaiser, S. T. J. "Passive telemetric readout system." IEEE Sensors Journal 6.5 (2006): 1340-1345.

Kashif F M, Verghese G C, Novak V, Czosnyka M, and Heldt T 2012 Model-based noninvasive estimation of intracranial pressure from cerebral blood flow velocity and arterial pressure Sci. Transl. Med. 4 129ra44

Kawoos U, Meng X, Huang S M, Rosen A, McCarron R M and Chavko M 2014 Telemetric intracranial pressure monitoring in blast-induced traumatic brain injury IEEE Trans. Biomed. Eng. 61 841–7

Kawoos U, Mugalodi G K, Tofighi M R, Neff S and Rosen A 2005 April A permanently implantable intracranial pressure monitor Proc. IEEE 31st Annu. Northeast Bioeng. Conf., 2005. 17–9

Kemp D T 1978 Stimulated acoustic emissions from within the human auditory system J. Acoust. Sci. Am. 64 1386–91

Kiefer M, Antes S, Leonhardt S, Schmitt M, Orakcioglu B, Sakowitz O W and Eymann R 2012 Telemetric ICP measurement with the first CE-approved device: data from animal experiments and initial clinical experiences Acta Neurochir. Suppl. 114 111–6

Kiening K L, Schoening W N, Stover J F and Unterberg A W 2003 Continuous monitoring of intracranial compliance after severe head injury: relation to data quality, intracranial pressure and brain tissue PO2 Brit. J. Neurosurg. 17 311–8

Kiening K L, Schoening W, Unterberg A W, Stover J F, Citerio G, Enblad P and Nilsson P 2005 Assessment of the relationship between age and continuous intracranial compliance In Intracranial Pressure and Brain Monitoring XII pp. (Springer; Vienna) 293–7

Kim, S., Kim, H. J., Park, J. S., & Yang, S. S. (2001, April). Telemetry silicon pressure sensor of lc resonance type. In Design, Test, Integration, and Packaging of MEMS/MOEMS 2001 (pp. 452-462). International Society for Optics and Photonics.

Koskinen L O D and Olivecrona M 2005 Clinical experience with the intraparenchymal intracranial pressure monitoring Codman MicroSensor system Neurosurgery 56 693–8

Lang J M, Beck J, Zimmermann M, Seifert V and Raabe A 2003 Clinical evaluation of intraparenchymal Spiegelberg pressure sensor Neurosurgery 52 1455–9

Langfitt T W, Weinstein J D, Kassell N F and Simeone F A 1964 Transmission of increased intracranial pressure. I. Within the craniospinal axis J. Neurosurg. 21 989–97

Larson M D and Muhiudeen I 1995 Pupillometric analysis of the 'absent light reflex' Arch. Neurol-Chicago 52 369–72

Law, Samuel K. "Thickness and resistivity variations over the upper surface of the human skull." Brain topography 6.2 (1993): 99-109.

Levoy M, "The Stanford volume data archive," ed, 2002.

Lenfeldt N, Koskinen L O, Bergenheim A T, Malm J and Eklund A 2007 CSF pressure assessed by lumbar puncture agrees with intracranial pressure Neurology 68 155–8

Lescot T, Reina V, Le Manach Y, Boroli F, Chauvet D, Boch A L and Puybasset L 2012 In vivo accuracy of two intraparenchymal intracranial pressure monitors Applied Physiology in Intensive Care Medicine 37 (Springer; Berlin Heidelberg) pp. 249–53

Levinsky A, Papyan S, Weinberg G, Stadheim T and Eide P K 2016. Non-invasive estimation of static and pulsatile intracranial pressure from transcranial acoustic signals. Med. Eng. Phys. 38 47784

Li Z and Luo Y 2010 Finite element study of correlation between intracranial pressure and external vibration responses of human head. Adv. Theor. Appl. Mech.3 139–49

Liebeskind D S, Marcinkevicius E, Pranevicius M, Pranevicius O, Ragauskas A, Matijosaitis V, Zakelis R, Petrikonis K, Rastenyte D, Piper I and Daubaris G 2013 Clinical assessment of noninvasive intracranial pressure absolute value measurement method Neurology 80 507–8

Lilja A, Andresen M, Hadi A, Christoffersen D and Juhler M 2014 Clinical experience with telemetric intracranial pressure monitoring in a Danish neurosurgical center Clin. Neurol. Neurosur. 120 36–40

Liu H, Wang W, Cheng F, Yuan Q, Yang J, Hu J and Ren G 2015 External ventricular drains versus intraparenchymal intracranial pressure monitors in traumatic brain injury: a prospective observational study World Neurosurg. 83 794–800

Lozier A P, Sciacca R R, Romagnoli M F and Connolly Jr E S 2002 Ventriculostomy-related infections: a critical review of the literature Neurosurgery 51 170–82

Luerssen T G 1997 Intracranial pressure: Current status in monitoring and management Semin. Pediatr. Neurol. 4 146–55

Mack W J, King R G, Ducruet A F, Kreiter K, Mocco J, Maghoub A, Mayer S and Connolly Jr E S 2003 Intracranial pressure following aneurysmal subarachnoid hemorrhage: monitoring practices and outcome data Neurosurg. Focus 14 1–5

Maloney-Wilensky E, Gracias V, Itkin A, Hoffman K, Bloom S, Yang W, Christian S and LeRoux PD 2009 Brain tissue oxygen and outcome after severe traumatic brain injury: A systematic review* Crit. Care Med. 37 2057–63

Marchbanks R J 1989 Method and apparatus for measuring intracranial fluid pressure U.S. Patent 4,841,986

Marioli, Daniele, et al. "A new measurement method for capacitance transducers in a distance compensated telemetric sensor system." Measurement Science and Technology 16.8 (2005): 1593.

Mayhall C G, Archer N H, Lamb V A, Spadora A C, Baggett J W, Ward J D, and Narayan R K 1984 Ventriculostomy-related infections New Engl. J. Med. 310 553–9

Medow. J Doctor's 2011 October 25 Madison doctor creates possible life-saving device for children with hydrocephalus Wisconsin State Journal

Meeker M, Du R, Bacchetti P, Privitera C M, Larson M D, Holland M C and Manley G 2005 Pupil examination: validity and clinical utility of an automated pupillometer J. Neurosci. Nurs. 37 34–40

Mertz K. Bencsik B, Büki B and Avan P 2004 Noninvasive testing of intracranial pressure changes due to body position in infants Orv Hetil. 145 1427–30

Meng, Xu, et al. "Dynamic evaluation of a digital wireless intracranial pressure sensor for the assessment of traumatic brain injury in a swine model." IEEE Transactions on Microwave Theory and Techniques 61.1 (2013): 316-325.

Michaeli D 2000 Noninvasive monitoring of intracranial pressure WO Patent 00068647

Michaeli D and Rappaport Z H 2002 Tissue resonance analysis: a novel method for noninvasive monitoring of intracranial pressure: Technical note J. Neurosurg. 96 1132–7

Mick E C 1991 Method and apparatus for the measurement of intracranial pressure U.S. Patent 5,074,310

Mick E C 1992 Method and apparatus for the measurement of intracranial pressure U.S. Patent 5,117,835

Miyake H, Ohta T, Kajimoto Y and Matsukawa M 1997 A new ventriculoperitoneal shunt with a telemetric intracranial pressure sensor: clinical experience in 94 patients with hydrocephalus Neurosurgery 40 931–5

Mokri B 2001 The Monro–Kellie hypothesis applications in CSF volume depletion Neurology 56 1746-8

Mohan, Sunderarajan S., et al. "Simple accurate expressions for planar spiral inductances." IEEE Journal of solid-state circuits 34.10 (1999): 1419-1424.

Morgalla M H, Cuno M, Mettenleiter H, Will BE, Krasznai L, Skalej M, Bitzer M and Grote E H 1997 ICP monitoring with a re-usable transducer: Experimental and clinical evaluation of the Gaeltec ICT/b pressure probe Acta Neurochir. 139 569–73

Muehlmann M, Koerte I K, Laubender R P, Steffinger D, Lehner M, Peraud A, Heinen F, Kiefer M, Reiser M and Ertl-Wagner B 2013 Magnetic resonance–based estimation of intracranial pressure correlates with ventriculoperitoneal shunt valve opening pressure setting in children with hydrocephalus Invest. Radiol. 48 543–7

Münch E C, Bauhuf C, Horn P, Roth H R, Schmiedek P and Vajkoczy P 2001 Therapy of malignant intracranial hypertension by controlled lumbar cerebrospinal fluid drainage Crit. Care Med. 29 976–81

Neagu, C. R., et al. "Characterization of a planar microcoil for implantable microsystems." Sensors and Actuators A: Physical 62.1-3 (1997): 599-611.

Nopper, Reinhard, Remigius Niekrawietz, and Leonhard Reindl. "Wireless readout of passive LC sensors." IEEE Transactions on Instrumentation and Measurement 59.9 (2010): 2450-2457.

Olzowy B, von Gleichenstein G, Canis M and Mees K 2008 Distortion product otoacoustic emissions for assessment of intracranial hypertension at extreme altitude? Eur. J. Appl. Physiol. 103 19–23

Park, E. C., Yoon, J. B., & Yoon, E. (1998). Hermetically sealed inductor-capacitor (LC) resonator for remote pressure monitoring. Japanese journal of applied physics, 37(12S), 7124.

Piper I 1997 Chapter 6 Intracranial pressure and elastance In Reilly P and Bullock R (eds) Head Injury. London: Chapman & Hall.

Piper I, Barnes A, Smith D and Dunn L 2001 The Camino intracranial pressure sensor: is it optimal technology? An internal audit with a review of current intracranial pressure monitoring technologies Neurosurgery 49 1158–65

Pople I K, Muhlbauer M S, Sanford R A and Kirk E 1995 Results and complications of intracranial pressure monitoring in 303 children Pediatr. Neurosurg. 23 64–7

Popovic D, Khoo M, and Lee S 2009 Noninvasive monitoring of intracranial pressure Recent Patents on Biomedical Engineering 2 165–79

Poupko B Z, Reichman Y, Rappaport A and Ben-Ari S. 2012 Non-invasive intracranial monitor U.S. Patent 8,211,031

Pranevicius O, Pranevicius M, Pranevicius H, Marcinkevicius E and Liebeskind D S 2012 Noninvasive method to measure intracranial and effective cerebral outflow pressure U.S. Patent 8,109,880

Quincke H 1891 Lumbalpunktion des hydrocephalus Berl. Klin. Wochenschr. 929–33

Raabe A, Totzauer R, Meyer O, Stöckel R, Hohrein D and Schöche J 1998 Reliability of epidural pressure measurement in clinical practice: behavior of three modern sensors during simultaneous ipsilateral intraventricular or intraparenchymal pressure measurement Neurosurgery 43 306–11

Raboel P H, Bartek J, Andresen M, Bellander B M, and Romner B 2012 Intracranial pressure monitoring: invasive versus non-invasive methods—a review Crit. Care Res. Pract. 2012 ID 950393

Ragauskas A 2006 Method and apparatus for noninvasive determination of the absolute value of intracranial pressure U.S. Patent 7,147,605

Ragauskas A, Bartusis L, Piper I, Zakelis R, Matijosaitis V, Petrikonis K and Rastenyte D 2014 Improved diagnostic value of a TCD-based non-invasive ICP measurement method compared with the sonographic ONSD method for detecting elevated intracranial pressure Neurol. Res. 36 607–14

Ragauskas A, Daubaris G, Dziugys A, Azelis V and Gedrimas V 2005 Innovative non-invasive method for absolute intracranial pressure measurement without calibration In Intracranial Pressure and Brain Monitoring XII (Springer; Vienna) pp. 357–61

Ragauskas A, Daubaris G, Petkus V, Ragaisis V and Ursino M 2005 Clinical study of continuous non-invasive cerebrovascular autoregulation monitoring in neurosurgical ICU In Intracranial Pressure and Brain Monitoring XII (Springer; Vienna) pp. 367–70

Ragauskas A, Daubaris G, Ragaisis V and Petkus V 2003 Implementation of non-invasive brain physiological monitoring concepts Med. Eng. Phys. 25 667–78

Ragauskas A, Matijosaitis V, Zakelis R, Petrikonis K, Rastenyte D, Piper I and Daubaris G 2012 Clinical assessment of noninvasive intracranial pressure absolute value measurement method Neurology 78 1684–91

Ragauskas A.and Daubaris G 1995 Method and apparatus for non-invasively deriving and indicating of dynamic characteristics of the human and animal intracranial media U.S. Patent 5,388,583

Rai P and Varadan V K 2010 March Organic electronics based pressure sensor towards intracranial pressure monitoring SPIE Smart Structures and Materials+ Nondestructive Evaluation and Health Monitoring 764617

Rajajee V, Vanaman M, Fletcher J J and Jacobs T L 2011 Optic nerve ultrasound for the detection of raised intracranial pressure Neurocrit. Care 15 506–15

Raju, Salahuddin, et al. "Modeling of mutual coupling between planar inductors in wireless power applications." IEEE Transactions on Power Electronics 29.1 (2014): 481-490.

Rangel-Castillo L, Gopinath S, and Robertson C S 2008 Management of intracranial hypertension Neurol. Clin. 26 521–41

Reina, M. A., Lopez-Garcia, A., Dittmann, M., & De Andrés, J. A. (1996). Structural analysis of the thickness of human dura mater with scanning electron microscopy. Revista espanola de anestesiologia y reanimacion, 43(4), 135-137.

Rosenfeld J G Watts C and York D H 1986 Method and apparatus for intracranial pressure estimation U.S. Patent 4,564,022

Ross N and Eynon C A 2005 Intracranial pressure monitoring Trends in Anaesthesia & Critical Care 16 255–61

Rossi S, Buzzi F, Paparella A, Mainini P and Stocchetti N 1998 Complications and safety associated with ICP monitoring: a study of 542 patients Acta Neurochir Suppl. 71 91–3

Saladino A, White J B, Wijdicks E F and Lanzino, G 2009 Malplacement of ventricular catheters by neurosurgeons: a single institution experience Neurocrit. Care 10 248–52

Schade R P, Schinkel J, Visser L G, Van Dijk J M C, Voormolen J H and Kuijper E J 2005 Bacterial meningitis caused by the use of ventricular or lumbar cerebrospinal fluid catheters J. Neurosurg. 102 229–34

Schmidt B, Czosnyka M, Raabe A, Yahya H, Schwarze J J, Sackerer D, Sander D and Klingelhöfer J 2003 Adaptive noninvasive assessment of intracranial pressure and cerebral autoregulation Stroke 34 84–9

Schmid, G., Neubauer, G., & Mazal, P. R. (2003). Dielectric properties of human brain tissue measured less than 10 h postmortem at frequencies from 800 to 2450 MHz. Bioelectromagnetics, 24(6), 423-430.

Schmutzhard J, Aregger FC, Otieno A, Bunk S, Zorowka P and Schmutzhard E 2013 Release of intracranial pressure leads to improvement of otoacoustic emissions–a case report of a Kenyan child with complicated tuberculous meningitis. J. Trop. Pediatr. 59: 326–9

Sinha D N 2000 Method for noninvasive intracranial pressure measurement U.S. Patent 6,117,089

Soldatos T, Karakitsos D, Chatzimichail K, Papathanasiou M, Gouliamos A and Karabinis A 2008 Optic nerve sonography in the diagnostic evaluation of adult brain injury Crit. Care 12 R67

Speck V, Staykov D, Huttner H B, Sauer R, Schwab S and Bardutzky J 2011 Lumbar catheter for monitoring of intracranial pressure in patients with post-hemorrhagic communicating hydrocephalus Neurocrit. Care 14 208–15

Stehlin E F, McCormick D, Malpas S C, Pontré B P, Heppner P A and Budgett D M 2015 MRI interactions of a fully implantable pressure monitoring device J. Magn. Reson. Imaging 42 14419

Steiner L A and Andrews P J D 2006 Monitoring the injured brain: ICP and CBF Brit. J. Anaesth. 97 26–38

Stendel R, Heidenreich J, Schilling A, Akhavan-Sigari R, Kurth R, Picht, T, Pietilä T, Suess O, Kern C, Meisel J and Brock M 2003 Clinical evaluation of a new intracranial pressure monitoring device Acta Neurochir. 145 185–93

Stettin E, Paulat K, Schulz C, Kunz U and Mauer U M 2011 Noninvasive intracranial pressure measurement using infrasonic emissions from the tympanic membrane J. Clin. Monitor. Comp. 25 203–10

Timoshenko, Stephen, and Sergius Woinowsky-Krieger. "Theory of plates and shells." (1959).

Tranquart F, Bergès O, Koskas P, Arsene S, Rossazza C, Pisella P J and Pourcelot L 2003 Color Doppler imaging of orbital vessels: personal experience and literature review J. Clin. Ultrasound 31 258–73

Troedsson, Niklas, and Henrik Sjöland. "A distributed capacitance analysis of co-planar inductors for a CMOS QVCO with varactor tuned buffer stage." Analog Integrated Circuits and Signal Processing 42.1 (2004): 7-19.

Tse T S, Cheng K F, Wong K S, Pang K Y and Wong C K 2010 Ventriculostomy and infection: a 4-year-review in a local hospital Surg Neurol Int. 1 47

Tsung J W, Blaivas M, Cooper A and Levick N R 2005 A rapid noninvasive method of detecting elevated intracranial pressure using bedside ocular ultrasound: application to 3 cases of head trauma in the pediatric emergency department Pediatr. Emerg. Care 21 94–8

Tuettenberg J, Czabanka M, Horn P, Woitzik J, Barth M, Thomé C, Vajkoczy P, Schmiedek P and Muench E 2009 Clinical evaluation of the safety and efficacy of lumbar cerebrospinal fluid drainage for the treatment of refractory increased intracranial pressure: Clinical article J. Neurosurg. 110 1200–8

Verweij B H, Muizelaar J P and Vias F C 2001 Hyperacute measurement of intracranial pressure, cerebral perfusion pressure, jugular venous oxygen saturation, and laser Doppler flowmetry, before and during removal of traumatic acute subdural hematoma J. Neurosurg. 95 569–72

Voss S E, Horton N J, Tabucchi T H, Folowosele F O and Shera C A 2006 Posture-induced changes in distortion-product otoacoustic emissions and the potential for noninvasive monitoring of changes in intracranial pressure Neurocrit. Care 4 251–7

Weerakkody R A, Czosnyka M, Zweifel C, Castellani G, Smielewski P, Keong N, Haubrich C, Pickard J and Czosnyka Z 2010 Slow vasogenic fluctuations of intracranial pressure and cerebral near infrared spectroscopy—an observational study Acta Neurochir. 152 1763–9

Welschehold S, Schmalhausen E, Dodier P, Vulcu S, Oertel J, Wagner W and Tschan C A 2012 First clinical results with a new telemetric intracranial pressure-monitoring system Neurosurgery 70 Suppl 44–9

Wen, P. Y., and S. K. Teoh. "Clinical presentation and diagnosis of brain tumors." Office practice of neurology. 2nd ed. Philadelphia: Churchill Livingstone (2003): 1013-7.

Wen-Teng, Chang, and Lai Su-Hao. "Measuring reactive near-field interference using the quartz oscillators intermodulation." Electronics, Control, Measurement, Signals and their Application to Mechatronics (ECMSM), 2015 IEEE International Workshop of. IEEE, 2015.

Wiegand C and Richards P 2007 Measurement of intracranial pressure in children: a critical review of current methods Dev. Med. Child Neurol. 49 935–41

Wu X and Ji Z 2007 Non-invasive detection for intracranial high pressure with FVEP picked-up by independent component analysis Sheng Wu Yi Xue Gong Cheng Xue Xa Zhi 24 1015–8

Yang J, Charif A C, Puskas J E, Phillips H, Shanahan K J, Garsed J, Fleischman A, Goldman K, Luebbers M T, Dombrowski S M and Luciano M G 2015 Biocompatibility evaluation of a thermoplastic rubber for wireless telemetric intracranial pressure sensor coating J. Mech. Behav. Biomed. 45 83–9

Yoon H J, Jung J M, Jeong J S and Yang S S 2004 Micro devices for a cerebrospinal fluid (CSF) shunt system Sensors Actuat. A-Phys. 110 68–76

York D H, Pulliam M W, Rosenfeld J G and Watts C 1981 Relationship between visual evoked potentials and intracranial pressure J. Neurosurg. 55 909–16

York D, Legan M, Benner S and Watts C 1984 Further studies with a noninvasive method of intracranial pressure estimation Neurosurgery 14 456–61

Yue X and Wang L 2009 Deformation of skull bone as intracranial pressure changing Afr. J. Biotechnol. 8 745–50

Yue X, Wang L, Sun S and Tong L 2008 Viscoelastic finite-element analysis of human skull-dura mater system as intracranial pressure changing Afr. J. Biotechnol. 7 689–95

Zhang B O and Li S B 2012 Cine-PC MR in assessment of cerebrospinal fluid velocity in the aqueduct of the midbrain correlated with intracranial pressure–Initial study Med. Hypotheses 78 227–30

Zhang X 2014 Intracranial Pressure Sensor Master of Science in Electrical and Computer Engineering, University of Wisconsin-Madison

Zhao Y L, Zhou J Y and Zhu G H 2005 Clinical experience with the noninvasive ICP monitoring system Intracranial Pressure and Brain Monitoring XII (Springer; Vienna) pp. 351–5

Zhong J, Dujovny M, Park H K, Perez E, Perlin A R and Diaz F G 2003 Advances in ICP monitoring techniques Neurol. Res. 25 339–50

Zweifel C, Castellani G, Czosnyka M, Helmy A, Manktelow A, Carrera E, Brady K M, Hutchinson P J, Menon D K, Pickard J D and Smielewski P 2010 Noninvasive monitoring of cerebrovascular reactivity with near infrared spectroscopy in head-injured patients J. Neurotraum. 27 1951-8.

Shmueli, G., Patel, N. R., & Bruce, P. C. (2011). Data mining for business intelligence: concepts, techniques, and applications in Microsoft Office Excel with XLMiner. John Wiley and Sons.

Elixmann, I. M., Goffin, C., Krueger, R., Meier, U., Lemcke, J., Kiefer, M., ... & Leonhardt, S. (2012, August). Case study of relevant pressures for an implanted hydrocephalus valve in everyday life. In Engineering in Medicine and Biology Society (EMBC), 2012 Annual International Conference of the IEEE (pp. 1635-1638). IEEE.

Portella, G., Cormio, M., Citerio, G. et al. Continuous cerebral compliance monitoring in severe head injury: its relationship with intracranial pressure and cerebral perfusion pressure. Acta Neurochir (Wien)147, 707–713 (2005). https://doi.org/10.1007/s00701-005-0537-z

G. Rodríguez-Boto, M. Rivero-Garvía, R. Gutiérrez-González, J. Márquez-Rivas, Basic concepts about brain pathophysiology and intracranial pressure monitoring, Neurología (English Edition), 2015

Bishop SM, Ercole A (2018) Multi-scale peak and trough detection optimised for periodic and quasi-periodic neuroscience data. Acta Nerochirurgica Suppl 126:189–195. https://doi.org/10.1007/978-3- 319-65798-1_39

Germon K (1988) Interpretation of ICP pulse waves to determine intracerebral compliance. J Neurosci Nurs 20:344–351. https://doi. org/10.1097/01376517-198812000-00004

Sakka L, Coll G, Chazal J. Anatomy and physiology of cerebrospinal fluid. Eur Ann Otorhinolaryngol Head Neck Dis. 2011 Dec;128(6):309-16.

Lauren N. Telano; Stephen Baker. Physiology, Cerebral Spinal Fluid, 2021

Mechanisms of fluid movement into, through and out of the brain: evaluation of the evidence

Preuss, M., et al. "Updated physiology and pathophysiology of CSF circulation—the pulsatile vector theory." Child's Nervous System 29.10 (2013): 1811-1825.

Rekate HL, Nadkarni TD, Wallace D (2008) The importance of the cortical subarachnoid space in understanding hydrocephalus. J Neurosurg Pediatr 2(1):1–11

Agarwal G., Berman B., Stark L. (1969) A lumped parameter model of the cerebrospinal fluid system. IEEE Trans Biomed Eng, 16, 45-53.

Takemae T., Kosugi Y., Ikebe J., Kumagai Y., Matsuyama K., Saito H. (1987) A simulation study of intracranial pressure increment using an electrical circuit model of cerebral circulation. IEEE Trans Biomed Eng, 34, 958-962.

Rekate H. L., Brodkey J. A., Chizeck H. J., el Sakka W., Ko W. H. (1988) Ventricular volume regulation: a mathematical model and computer simulation. Pediatr Neurosci, 14, 77-84.

Stevens S. A., Stimpson J., Lakin W. D., Thakore N. J., Penar P. L. (2008) A model for idiopathic intracranial hypertension and associated pathological ICP wave-forms. IEEE Trans Biomed Eng, 55, 388-398.

Spector R, Robert Snodgrass S, Johanson CE. A balanced view of the cerebrospinal fluid composition and functions: Focus on adult humans. Exp Neurol. 2015 Nov;273:57-68.

Lutz, Barry R et al. “New and improved ways to treat hydrocephalus: Pursuit of a smart shunt.” Surgical neurology international vol. 4,Suppl 1 S38-50. 19 Mar. 2013, doi:10.4103/2152-7806.109197

Kazimierska, Agnieszka et al. “Compliance of the cerebrospinal space: comparison of three methods.” Acta neurochirurgica vol. 163,7 (2021): 1979-1989. doi:10.1007/s00701-021-04834-y

Dai, Honghao & Jia, Xiaodong & Pahren, Laura & Lee, Jay & Foreman, Brandon. (2020). Intracranial Pressure Monitoring Signals After Traumatic Brain Injury: A Narrative Overview and Conceptual Data Science Framework. Frontiers in Neurology. 11. 10.3389/fneur.2020.00959.

Carrera E, Kim DJ, Castellani G, Zweifel C, Czosnyka Z, Kasparowicz M, Smielewski P, Pickard JD, Czosnyka M. What shapes pulse amplitude of intracranial pressure? J Neurotrauma. 2010 Feb;27(2):317-24. doi: 10.1089/neu.2009.0951. PMID: 19852586.

Eide P.K.Brean A.2006Intracranial pulse pressure amplitude levels determined during preoperative assessment of subjects with possible idiopathic normal pressure hydrocephalusActa Neurochir. (Wien.)1481151-1156; discussion 6.Eide, P.K., and Brean, A. (2006). Intracranial pulse pressure amplitude levels determined during preoperative assessment of subjects with possible idiopathic normal pressure hydrocephalus. Acta Neurochir. (Wien.) 148, 1151–1156; discussion 6.

Eide P.K.Sorteberg W.2006Intracranial pressure levels and single wave amplitudes, Glasgow Coma Score and Glasgow Outcome Score after subarachnoid haemorrhageActa Neurochir. (Wien.)1481267-1275discussion 75–76.Eide, P.K., and Sorteberg, W. (2006). Intracranial pressure levels and single wave amplitudes, Glasgow Coma Score and Glasgow Outcome Score after subarachnoid haemorrhage. Acta Neurochir. (Wien.) 148, 1267–1275; discussion 75–76.

Holm S.Eide P.K.2008The frequency domain versus time domain methods for processing of intracranial pressure (ICP) signalsMed. Eng. Phys.30164-170.Holm, S., and Eide, P.K. (2008). The frequency domain versus time domain methods for processing of intracranial pressure (ICP) signals. Med. Eng. Phys. 30, 164–170.

Elixmann IM, Hansinger J, Goffin C, Antes S, Radermacher K, Leonhardt S. Single pulse analysis of intracranial pressure for a hydrocephalus implant. Annu Int Conf IEEE Eng Med Biol Soc. 2012;2012:3939-42. doi: 10.1109/EMBC.2012.6346828. PMID: 23366789.

Elixmann IM, Walter M, Kiefer M, Leonhardt S. Simulation of existing and future electromechanical shunt valves in combination with a model for brain fluid dynamics. Acta Neurochir Suppl. 2012;113:77-81. doi: 10.1007/978-3-7091-0923-6_16. PMID: 22116428.

Elixmann IM, Goffin C, Krueger R, Meier U, Lemcke J, Kiefer M, Antes S, Leonhardt S. Case study of relevant pressures for an implanted hydrocephalus valve in everyday life. Annu Int Conf IEEE Eng Med Biol Soc. 2012;2012:1635-8. doi: 10.1109/EMBC.2012.6346259. PMID: 23366220.

Portella, G., Cormio, M., Citerio, G., Contant, C., Kiening, K., Enblad, P., & Piper, I. (2005). Continuous cerebral compliance monitoring in severe head injury: its relationship with intracranial pressure and cerebral perfusion pressure. Acta neurochirurgica, 147, 707-713. doi: 10.1007/s00701-005-0537-z

Shulman, K. and Marmarou, A. (1971), Pressure-Volume Considerations in Infantile Hydrocephalus. Developmental Medicine & Child Neurology, 13: 90-95. https://doi.org/10.1111/j.1469-8749.1971.tb03304.x

Marmarou A, Shulman K, LaMorgese J. Compartmental analysis of compliance and outflow resistance of the cerebrospinal fluid system. J Neurosurg. 1975 Nov;43(5):523-34. doi: 10.3171/jns.1975.43.5.0523. PMID: 1181384.

Vennemann B, Obrist D, Rösgen T. A smartphone-enabled wireless and batteryless implantable blood flow sensor for remote monitoring of prosthetic heart valve function. PLoS One. 2020 Jan

14;15(1):e0227372. doi: 10.1371/journal.pone.0227372. PMID: 31935231; PMCID: PMC6959614.